Radiation Measurements 130 (2020) 106228

Contents lists available at ScienceDirect

Radiation Measurements

journal homepage: http://www.elsevier.com/locate/radmeas

Review

Unique capabilities and applications of Microchannel Plate (MCP) detectors with Medipix/Timepix readout

A.S. Tremsin *, J.V. Vallerga

Space Sciences Laboratory, University of California at Berkeley, Berkeley, CA, 94720, USA

ARTICLE INFO

Keywords:
Medipix/timepix readout
Microchannel plates
Event counting detectors
Neutron imaging
Photon counting

ABSTRACT

The development of highly pixelated fast Medipix/Timepix readout enabled a large number of novel hybrid detectors, where incoming particles/photons are initially converted into a measureable charge, typically exceeding 1000 electrons. Among those possible converters are Microchannel plate (MCP) electron multipliers, which provide some unique capabilities when combined with bare Medipix/Timepix readout. Fast event multiplication with ~10–20 ps time jitter, localized within the MCP pore (typically 5–10 μm in diameter) and low dark currents make MCP/Medipix/Timepix hybrid devices very attractive for the high spatial and temporal resolution detection of low energy photons (soft X-ray, UV and visible), alpha particles, ions and also neutrons. In this review we present a brief overview of the capabilities of MCP/Medipix/Timepix detectors and show the results of experiments conducted with such hybrid detectors in various applications including neutron imaging, astronomy, mass spectroscopy and others.

1. Introduction

High resolution event counting detectors require conversion of incoming particle into some sort of detectable signal (e.g. light produced by scintillators, heat converted into measurable change in resistance in superconducting devices, charge created in solid state sensors upon absorption of an energetic particle, etc.), which eventually is registered electronically. The Medipix/Timepix readout integrated circuit (ROIC) (Llopart et al., 2002), (Llopart et al., 2007), (Poikela et al., 2014) requires charge of few thousand electrons to register an event in a pixel with all internally generated noise reliably thresholded. Detection of x-rays above ~10 keV, alpha particles, energetic electrons, and ions can be based on the conversion of these incoming particles into electron/-hole pairs and subsequent charge transfer to collection electrodes within a solid converter attached to a Medipix/Timeipx ROIC. However, detection of low energy particles, such as soft X-ray, UV and visible photons, requires signal amplification, which can be done by various types of charge amplifier before it is reliably detected by a Medipix/Timepix readout. In this paper we describe the technology and its applications, where the particle detection and subsequent event amplification is performed by a microchannel plate (MCP) amplifier (Wiza, 1979) followed by the event encoding by a Medipix/Timepix pixelated readout.

1.1. Event counting detectors with microchannel plates

Detectors with microchannel plates (MCPs) are widely used at the present time in the applications where photon/particle counting with high spatial (~10–20 μm) and temporal resolution (~10–50 ps) with low readout noise and high dynamic range is required. The incoming photon/particle is converted into an electron, which is then amplified to $\sim 10^3$-10^7 electrons by a single MCP or a stack of several MCPs, biased at voltages usually at ~1 kV per microchannel plate. Various techniques for the conversion into initial electron can be employed: photocathodes are typically used for the detection of soft X-rays, UV and visible light photons, while alpha particles, ions and electrons produce a secondary electron upon interaction with the input surface of the MCP, usually coated with a thin nichrome electrode. Detection of neutrons relies on production of secondary electrons by the products of neutron absorption reaction within the glass bulk, doped with ^{10}B and ^{nat}Gd atoms. Once the electron is produced within or just above the MCP pore, its amplification processes is constrained to a single pore (or several pores in case of a stacked MCPs configuration) limiting charge spreading to a very small area. The process of amplification typically takes less than a nanosecond and the time jitter of the output electron cloud is typically on the scale of 10–25 ps for the present generation of conventional microchannel plates with 5–10 μm pores. The resulting electron cloud produced for every

* Corresponding author.
E-mail address: ast@ssl.berkeley.edu (A.S. Tremsin).

https://doi.org/10.1016/j.radmeas.2019.106228
Received 27 February 2019; Accepted 7 December 2019
Available online 11 December 2019

incoming particle is encoded by various types of readout anodes, which either utilize charge division or charge propagation time to encode the position of each event (e.g. Wedge Strip Zig (Siegmund et al., 1986), Cross Delay Line (Siegmund et al., 1999), Cross Strip (Siegmund et al., 2003) readouts) or localize the event to a single pad of the readout anode (e. g. multianode Photo Multiplier Tubes (PMTs) (Inami et al., 2008)). The large signal produced for every particle enables even counting with virtually no readout noise as all the thermal noise of readout electronics can be thresholded. The schematic diagram of an MCP detector is shown in Fig. 1. The photocathode can be deposited both on the input window of a detector or directly on the MCP, while for the electron, ion and alpha detection these devices are placed directly into vacuum without any input windows. Different types of readout can be implemented for the event encoding and there is no one *ideal* readout, which can meet the requirements of all the applications. A compromise between the spatial and temporal resolution, event counting rate, detector active area, lifetime and other parameters needs to be found for a particular application. Initially, most event counting MCP detectors were built for relatively low input counting rates, not exceeding ~0.5 MHz per detector, while event rates as low as 0.1 cnt/cm^2/sec were still possible, corresponding to dynamic range of ~10^6. Recent progress in the readout electronics substantially extended the counting rate capabilities of MCP detectors to event rates as high as ~500 MHz with the pixelated readout configurations, operating many readout channels in parallel.

1.2. Medipix/Timepix readout in MCP detectors

One of those novel readout configuration was the implementation of Medpix/Timepix Application Specific Integrated Circuits (ASICs) developed within the Medipix collaboration (Llopart et al., 2002), (Llopart et al., 2007), (Poikela et al., 2014). Different from the majority of Medipix/Timepix hybrid detection devices, where the conversion of incoming particle into measurable charge is performed by a solid state converter (e.g. Si, CdTe, CdZnTe, GaAs) (Ballabriga et al., 2018), bump bonded to a Medipix/Timepix ASIC, detectors with microchannel plates utilize bare Medipix/Timepix chips, placed in vacuum in close proximity

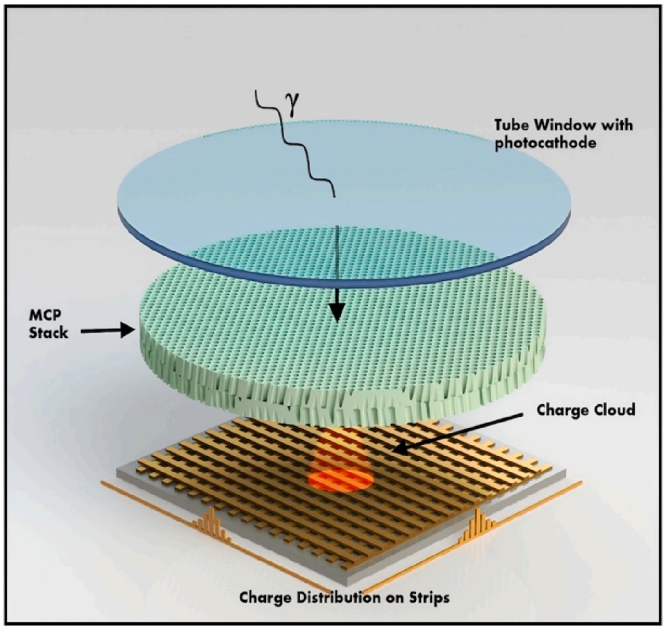

Fig. 1. Schematic representation of a detector with a Microchannel Plate amplifier, where incoming particles (photons, ions, electrons, alphas, neutrons) are first converted into electrons, then amplified by a factor of 10^3-10^7 and subsequently encoded by a certain type of readout, which can be an array of bare Medipix/Timepix chips (Siegmund et al., 2014).

to a stack of MCPs. The MCP electron cloud impinge directly on the metalization pads of the Medipix/Timepix chip. The distance between the MCP and the readout and the electric field in between them determine the spread of the charge between several pixels. At the MCP output surface the charge is typically localized within ~6–30 μm, enabling event encoding with 1–2 pixel accuracy. However, in some cases, sub-pixel resolution can be achieved by spreading the charge over several pixels and by calculation of the centroid for each detected charge cluster (Tremsin et al., 2012a), improving spatial resolution of MCP/Timepix detectors to the spacing of the MCP pores. Spatial resolution of ~7 μm resolution has been demonstrated with such devices (Tremsin et al., 2018a) and as low as ~5 μm with another type of pixelated readout (Bellazzini et al., 2008), although the counting rate capabilities of such detector are reduced as the overlaps between the single particle clusters should be avoided for the proper event encoding.

1.3. Advantages and disadvantages of Medipix/Timepix readouts in MCP detectors

In this paper, we describe the unique capabilities and applications enabled by detection devices utilizing MCP event amplification and signal encoding by a Medipix or Timepix readout. These unique detection capabilities have certain drawbacks, compared to solid-state hybrid Medipix/Timepix detectors. First of all, MCP detectors have to operate in vacuum and they require application of high voltages, typically ~3 kV per detector. Therefore the challenge of heat dissipation from Medipix/Timepix readouts need to be addressed in such detectors. Another disadvantage is in the fact that the gap between the chips becomes a dead area in MCP/Medipix/Timepix detectors. The information about the energy of incoming particle is also lost in the process of event amplification in the MCP, where the number of output electrons is not always linearly proportional to the number of input electrons due to saturation effects.

One of the major advantages of incorporation of Medipix/Timepix readout in MCP detectors is the substantial increase of counting rate capability as each pixel in the readout is an independent counter, enabling ~ GHz rates for a 28 × 28 mm^2 detector operating in event counting mode. At the same time, many simultaneous events can be encoded by the pixelated readout, which was not possible with most of the conventional high resolution MCP detectors (except for multianode PMTs, with very limited spatial resolution and a very large number of electronics channels). Another major improvement for the MCP detection technology is a substantial reduction of MCP gain, required for the detection of incoming particles. Due to the relatively low noise level in each pixel amplifier of a Medipix/Timepix readout (typically 75 e−rms), the output charge value of ~10^4 electrons is sufficient for the low noise detection of individual particles, a factor of 10–1000 lower compared to charge division or time propagation readouts used in MCP detectors. The reduced gain also leads to a substantial increase of local count rate capabilities (faster recharge time of the depleted MCP pore) and longer lifetime of the MCP detector, which is proportional to the extracted charge per given MCP area. However, until 4-side buttable Timepix4 readout becomes available, the active area of MCP/Medipix/Timepix detectors will be restricted to 2xN chip configurations, limiting the active area of such detectors compared to large devices possible with other types of readout (e.g. 20 × 20 cm^2 with XDL and strip line readouts (Siegmund et al., 2014), (Adams et al., 2015)). The power consumption per square cm is also quite high for the Medipix/Timepix devices compared to conventional anodes used in the past, where only 3 or 4 amplification and digitization channels are needed. Therefore as stated earlier, MCP detectors with Medpix/Timepix readout are very attractive for the applications with relatively high input counting rates or for the applications where multiple simultaneous particles need to be detected at the same time.

2. Applications of MCP/Medipix/Timepix detectors

The unique capability of microchannel plate amplifiers to convert an incoming single electron into a measurable charge of 10^3-10^7 electrons, preserving its location within 6–30 μm and with time jitter of only 10–20 ps enables accurate event detection of incoming particles as long as they can be converted into a single electron (e.g by a photoelectric effect) or even better few electrons. The efficiency of that conversion determined the ultimate sensitivity of MCP/Medipix/Timeipx detector. In this paper we demonstrate few novel capabilities provided by the combination of MCP amplifier and Medipix/Timepix pixelated readout, enabling event counting of low energy particles at high input fluxes, sometimes with many of them arriving nearly simultaneously.

2.1. Photon counting applications

Low noise photon counting with MCP detectors has been widely used in many applications ranging from Astrophysical instrumentation (Fraser, 2001), (Siegmund et al., 2004), to soft X-ray synchrotron instrumentation (Tremsin et al., 2007), to biological imaging (Michalet et al., 1611), (Hirvonen et al., 2017) and many others. For the detection of visible light photons microchannel plate photomultiplier tubes (MCP-PMT) are used where various types of readout are enclosed into a sealed vacuum tube. Multianode MCP-PMTs are commercially available and perform really well with the exception on the spatial resolution, which is limited by the size of the anode pad (Inami et al., 2008). Incorporation of Timepix readout into a sealed tube substantially increases the spatial resolution of these devices, as it was demonstrated recently (Vallerga et al., 2014). Schematic diagram of MCP photon counting detector with Timepix readout is shown in Fig. 2, where a drop face window is coated with a photocathode and installed in proximity to the MCP stack, followed by the Timepix readout. The electrical signals from the Timepix chips are transferred through vacuum feedthroughs on the back flange of the detector. The first sealed tube MCP detector containing a quad assembly of Timepix readout was produced with the input window positioned at non-optimal few mm gap above the MCP, substantially reducing the spatial resolution of the detector due to translational drift of photoelectrons between the photocathode and the MCP. However, that device demonstrated the fact that Timepix readout can sustain the tube manufacturing processes (which include 350° bakeout). Originally that detector technology was developed at the University of California at Berkeley for the adaptive optics applications (Vallerga et al., 2004), (Vallerga et al., 2005a), (Vallerga et al., 2005b). The possibility to perform photon counting in each pixel and read the entire image at a kHz frame rates made these detectors to be attractive candidates for the Shack–Hartmann style wavefront sensing applications. Among the many possible uses of such detector is the possibility to perform time-resolved imaging with timing resolution limited at the present time by the resolution of Timeix readout (~10 ns for Timepix (Llopart et al., 2007), ~1.56 ns for Timepix3 (Poikela et al., 2014) and expected ~200 ps for next generation Timepix4 being designed within the Medipix collaboration at the present time (Llopart et al., 2019)). Fig. 3 demonstrates the capabilities of time-resolved imaging, where AC phase of each individual light can be extracted from the measured data set consisting of thousands of time-resolved images time-tagged relative to 60 Hz AC power line (Vallerga et al., 2014). The three separate ac phases are easily distinguishable as shown in Fig. 2 c by the intensity curves of three individual lights extracted from data set of Fig. 2 b. The spatial resolution of MCP/Timepix detector is inferior compared to a regular commercial camera image of Fig. 2 a (partially due to non-ideal large gap between the photocathode and MCP), but the possibility to time tag every photon with high timing resolution and high sensitivity of MCP/Timepix detector enabling operation at very low light levels can be very attractive for some applications, including lidar 3D imaging. The expected 200 ps resolution of Timepix4 readout will substantially increase the possible application of MCP detectors with Timepix readout (Fiorini et al., 2018), including application in biological imaging such as Fluorescence Lifetime Imaging and Förster Resonance Energy Transfer (Michalet et al., 1611), (Hirvonen et al., 2017). Such devices will be able to encode the visible photons generated by scintillating materials in gamma ray and fast neutron imaging applications (e.g. homeland security, positron emission tomography), quantum optics (Just et al., 2014), solar flare imaging and many other applications.

2.2. Neutron imaging

Neutron imaging experiments with Medpix/Timepix readout were pioneered by Czech Technical University in Prague (Jakubek et al., 2006). The detection efficiency in these devices was limited to ~5% for thermal neutrons by the thickness of the neutron absorption layer deposited on a Si sensor: the thickness of that layer needs to be large enough for neutron absorption, but thin enough to allow reaction products to escape that layer and reach the sensor. The invention of neutron sensitive microchannel plates, suggested by Prof. Fraser (1995) and developed and manufactured by Nova Scientific, Inc. enabled novel class of neutron counting detectors, where MCPs are used for the conversion of incoming neutrons into an electron with very high detection efficiency of ~50% for thermal and 70% for cold neutrons (Tremsin et al., 2010a). Combination of such MCPs with Timepix readout substantially increased the counting rate capabilities of MCP neutron detectors and enabled a new class of energy-resolved neutron imaging experiments at spallation neutron sources. One of the very attractive features of MCP/Timepix detection devices is the possibility to time tag every neutron with high accuracy determined by the depth of neutron absorption within the MCP (~1 mm). For thermal neutrons that transfers to ~0.5 μs, while for the epithermal neutrons it can be as short as a few ns. Compared to other existing neutron counting technologies, MCP/Timepix detectors provide the unique combination of high counting rates, high detection efficiency and high spatial and temporal resolution, not achievable yet by other technologies. Gaseous detection devices, for example, are limited in counting rates and have slightly worse spatial resolution, although they allow much large active areas of

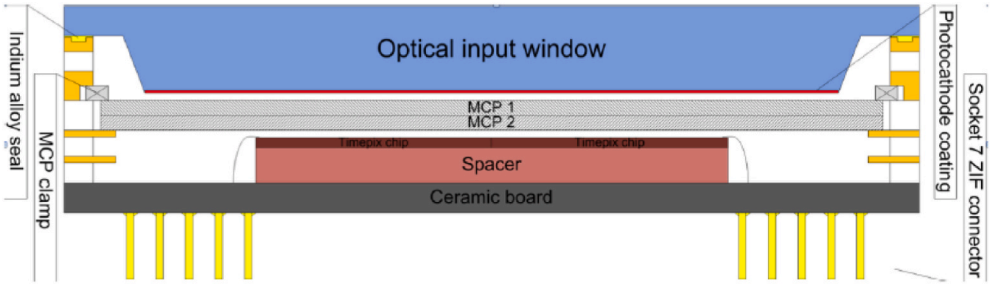

Fig. 2. A schematic cutaway of the Quad Timepix vacuum tube showing a drop-face window with a proximity focused photocathode directly above a chevron MCP pair. A ceramic spacer is used in that tube to elevate the 2 × 2 Timepix array to achieve the close (~500 μm) gap to the MCP output surface, while still using the existing mechanical format. The Timepix ASICs are wirebonded to the ceramic header (Vallerga et al., 2014).

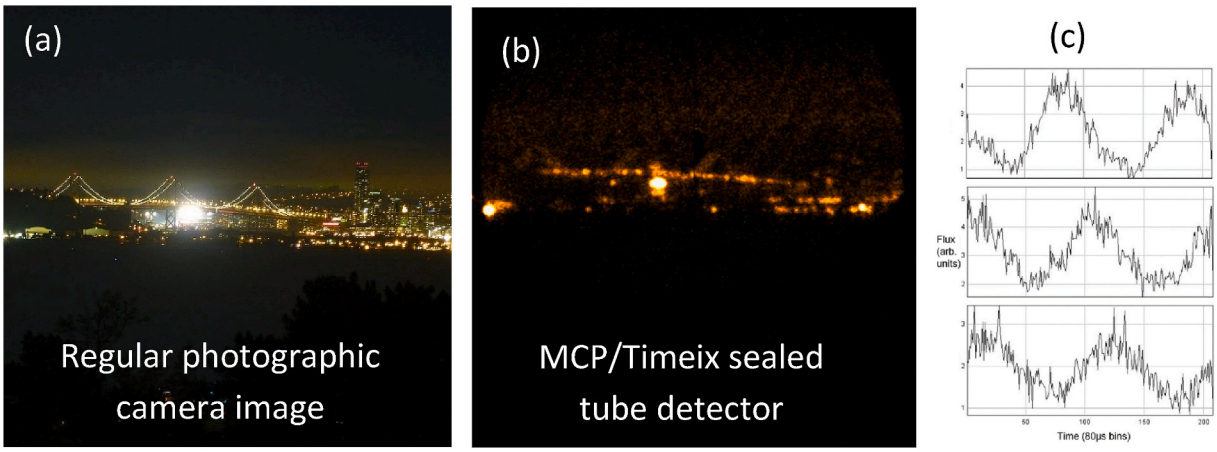

Fig. 3. (a) The photograph of the area imaged in time-resolved mode shown in (b). A commercial photographic camera provides much higher resolution than MCP/Timepix sealed tube detector, where non-optimal large photocathode-to-MCP gap introduced image blurring. (b) An individual slice (~80 μs wide) of a time-resolved imaging data set acquired over multiple periods of 60 Hz AC power. (c) Light curves from 3 different pixels of the time-resolved imaging data set shown in (b). The periodic intensity fluctuation is due to the AC power grid voltage (60 Hz) and three different phases separated by 120°. Peak to peak period is 8.33 ms (Vallerga et al., 2014).

10 × 10 cm^2 (Parker et al., 2013). Scintillator-based devices have very high spatial resolution and can register very high input fluxes, but are limited in their timing resolution by both long decay time of scintillation screens and the time resolution of the frame-based camera devices. At the present time MCP/Timepix detectors are used among a suite of other devices in the user program at several neutron imaging facilities (Tremsin et al., 2013a), (Nelson et al., 2018), (Santodonato et al., 2015), (Kockelmann et al., 2018). As usual, there is no one detector technology which can meet all the diverse needs of various neutron imaging experiments and the best detection technology should be determined for a specific experiment.

The results presented in this section were obtained with an MCP/Timepix detector developed by the University of California in collaboration with Nova Scientific and Techne Instruments with great help from the Medipix collaboration. The schematic diagram of detector used in neutron imaging experiments is shown in Fig. 4 (Tremsin et al., 2013b), (Tremsin et al., 2015a). A quad array of Timepix readout chips in that detector limited the active area to 28 × 28 mm^2. The detector is enclosed in an aluminium container, actively pumped by a turbomolecular pump to pressures of ~10^{-6} Torr. The data from the detector is transferred out of vacuum container over 128 data lines operating at 100 MHz during readout, enabling frame readout time of ~320 μs. The time of neutron arrival within each frame is registered relative to external trigger, if needed, when the Timepix readout is programmed to operate in Time of Arrival mode, where only one neutron per pixel per frame for that generation of Timepix readout is possible.

2.2.1. *White spectrum radiography and tomography*

The unique capabilities of neutrons to penetrate metals and to reveal organic materials is demonstrated in Fig. 5, where gun powder grains encapsulated in metal casing are imaged in tomographic mode (Tremsin et al., 2011a). Individual grains of powder can be visualized non-destructively by neutron imaging with ~110 μm spatial resolution determined by Timepix 55 μm pixels. The fast neutron counting at the

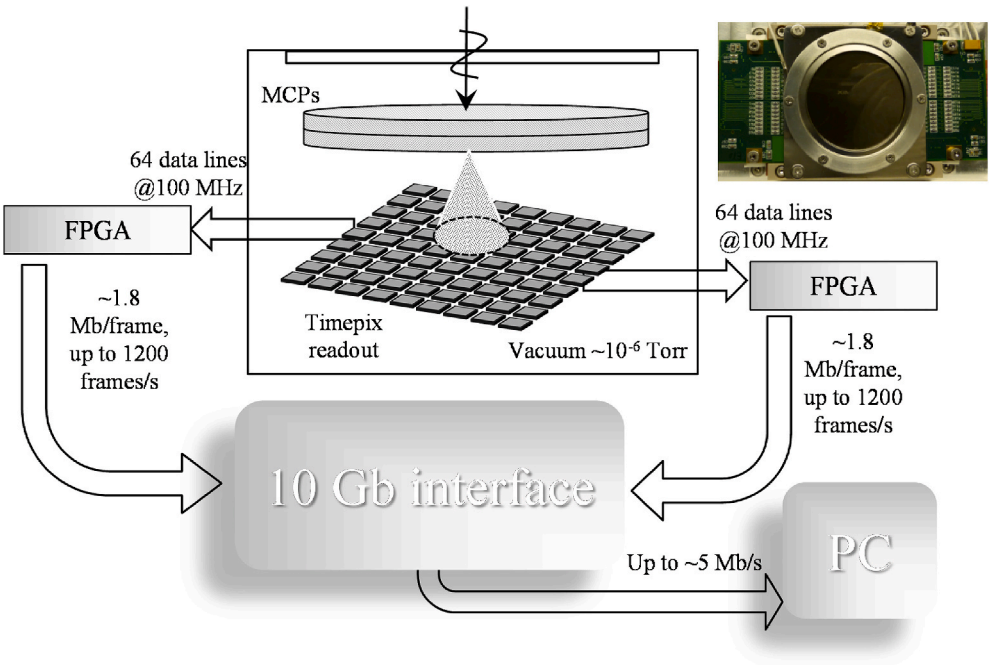

Fig. 4. Schematic diagram of the MCP/quad Timepix detector used in neutron imaging experiments. A chevron stack of MCPs converts incoming neutrons into secondary electrons through ^{10}B neutron absorption reaction and amplifies them to 10^4-10^5 output electrons per incoming neutron. The bare Timepix chips are placed in proximity to the MCP stack. The signals are transferred out of vacuum over a short cable and then subsequently transferred to PC over a 10 Gb interface (Tremsin et al., 2015a).

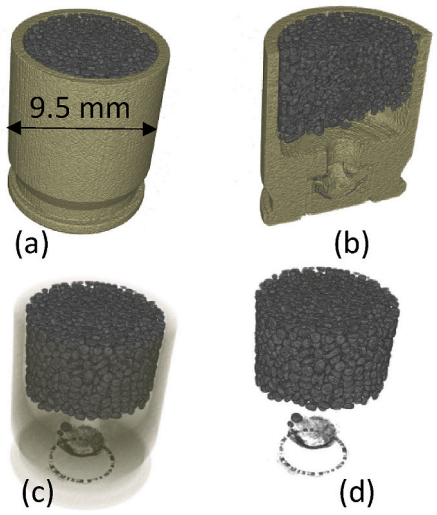

Fig. 5. Tomographic reconstruction of gunpowder encapsulated in a metal casing (a bullet). The gunpowder is distinguished from the metal casing by the difference in the neutron absorption coefficient. The metal is removed from the reconstruction in images (c) and (d). The shapes of single grains of ~400 μm in size are well resolved (Tremsin et al., 2011a).

rates exceeding 500 MHz were achieved with such detector operating in event counting mode. That high rate capability proved to be crucial for the white-beam imaging experiments in order to acquire sufficient neutron statistics per each pixel and to take full advantage of bright neutron sources built and commissioned over the last decade.

High spatial resolution imaging with sub-15 μm resolution has been also demonstrated with MCP/Timepx detectors by encoding the location of each neutron with sub-pixel accuracy through event centroiding (Tremsin et al., 2012a). The resolution in these images was limited by the size of the MCP pore, while the Timepix readout allowed event encoding to ~3–4 μm accuracy.

The possibility to quantify hydrogen content in various samples is one of the most attractive features of white-beam neutron radiography, where high scattering cross section of hydrogen atoms compared to many metals makes neutrons to be unique probes for such imaging experiments. Non-destructive quantification of hydrogen content in zirconia alloys, for example, which can be done to ~10 ppm accuracy, is very important for the studies of materials for future power reactors. MCP/Timepix detector was used for quantitative mapping of hydrogen content in multiple experiments conducted at several neutron sources (Tremsin et al., 2015b), (Buitrago et al., 2018).

Mapping water content in concrete samples has also been performed with MCP/Timepix neutron detector (Tremsin et al., 2015c), including the studies of ancient Roman concrete samples (Tremsin et al., 2019a), as demonstrated in Fig. 6. The possibility to map the water content within the bulk of concrete samples, nondestructively, with high spatial resolution in both 2D (as shown in Fig. 6) as well as in 3D through tomographic reconstruction demonstrates the unique capabilities of neutron imaging for the studies of various materials and structures, including imaging Li content in Li ion batteries and hydrogen distribution in fuel cells.

2.2.2. *Imaging of dynamic processes*

One of the most attractive features of MCP/Timpiex neutron counting detector is its ability to time tag every detected neutron (time of arrival Timepix mode) or to image at frame rates up to 1200 frames/sec with no readout noise. The latter is very important for neutron imaging experiments conducted with the limited neutron flux (compared to modern X-ray sources, for example, where intensity is orders of magnitude higher than in neutron imaging beamlines of 10^6-10^8 n/cm^2/s). No afterglow or time-delayed response exist in the MCP/Timepix detectors, which allows imaging to sub-μs timing resolution as demonstrated later in this paper.

Not only the static distribution of water, but also real-time imaging of water penetration into materials was visualized by neutron imaging experiments with MCP/Timepix detector, where the high frame rate capability, high detection efficiency and imaging with no readout noise were crucial for the success of these experiments (Cheng et al., 2015). The frames with image integration time of ~50 ms were acquired consecutively in order to quantify the speed of water penetration into a crack in a shale sample. The studied interaction of water, oil or other hydrogen-containing substances with various rock samples is important for the fracking oil extraction industry.

Dynamics of fuel injection from a diesel injector nozzle was also investigated with MCP/Timepix detectors, where cavitation within the injection nozzle is studied by neutron imaging for the nozzle operating at 10–25 Hz injection frequency (Tremsin et al., 2010b). The challenge of high pressure fuel injection and, most important, very small diameter of ~100 μm of the injection channel are being addressed in these experiments. While the fuel spray itself can be visualized by other imaging methods (e.g. by installing a small camera in the cylinder of the engine), the fuel transport within a steel injector cannot be studied in-situ by other techniques, making neutron imaging a unique method for these experiments. Another example of repetitive process studied with an MCP/Timepix neutron counting detector was mapping of water distribution within a small steam engine made of steel. Dynamics of water condensation and its movement the engine operating at 10 Hz frequency was also visualized (Tremsin et al., 2015d).

One of the unique features of neutron imaging is its capability to map the magnetic field distribution. This imaging is enabled by the fact that neutron spin precesses in the presence of a magnetic field. Earlier an imaging of static magnetic fields was performed with an integrating type of neutron detector (Kardjilov et al., 2008). However, imaging of a dynamic magnetic field was not possible with a slow integrating device. Here we show the result of dynamic imaging of an AC magnetic field, varied at 3 kHz frequency. The map of magnetic field in 2D was reconstructed from the measured neutron intensity variation obtained at the experimental setup shown in Fig. 7 a (Tremsin et al., 2015e). A

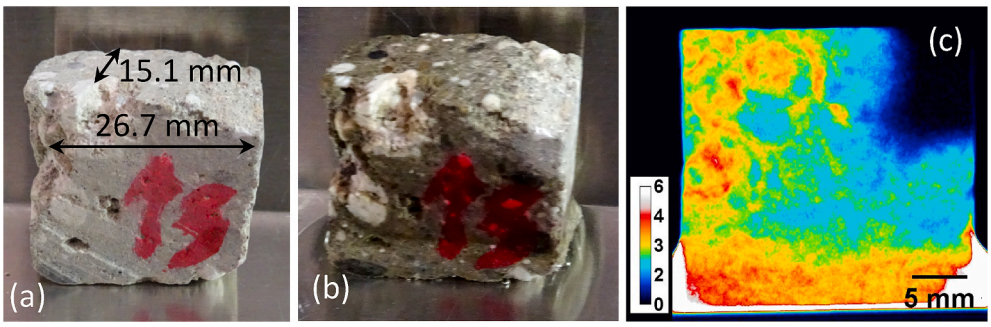

Fig. 6. Photograph of a dry concrete sample from ancient Roman city of Cosa (southern Tuscany) used in the experiment. (b) The same sample after absorption of water by capillary action (sample was partially immersed in water at the bottom). (c) Map of effective water thickness in wet Cosa concrete sample, reconstructed from the measured neutron transmission spectra. The color bar indicates the reconstructed water thickness in mm (Tremsin et al., 2019a). (For interpretation of the references to color in this figure legend, the reader is referred to the Web version of this article.)

polarized neutron beam passed through the region where a 3 kHz AC magnetic field was produced by a 15-loop coil, made of aluminium wire (nearly transparent to neutrons). The precession of neutron spin in the magnetic field resulted in intensity modulation after neutrons passed the spin analyzer placed in front of the detector. The 10μs-wide slices integrated over a particular phase of the 3 kHz process are shown in Fig. 7 b. Multiple periods of the 3 kHz process were integrated and wrapped into one stack of 10 μs-wide images in our experiment in order to acquire sufficient neutron counts per image. The repetitiveness of measured process was crucial for the latter wrapping and obviously cannot be implemented in case the process under investigation is not periodic, such as water propagation shown earlier. All time-slices of the AC process were acquired in one experiment with our detector, while time-gated devices would require scanning through all the phases imaged one at a time, wasting a large fraction of neutron flux. The images shown in Fig. 7 b are 2-dimensional integrals of the magnetic field produced by the coil. The possibility to reconstruct a 3-dimensional magnetic field distribution was also demonstrated recently with an MCP/Timepix detector installed at a pulsed neutron beamline (Sales et al., 2018), as well as by other method implemented at a continuous neutron source (Hilger et al., 2018).

Imaging of magnetic domains in transformer steel has also been performed for magnetic fields varying at 10 Hz frequency, Fig. 8 (Harti et al., 2018). The unique capability of neutrons to visualize these domains without stripping off the protective insulation enables studies of how the stresses introduced by the insulation coating can affect the dynamics of these domains, not possible with other domain visualization techniques at the present time.

2.2.3. *Energy-resolved imaging at pulsed sources*

Energy-resolved neutron imaging can be implemented both at continuous sources by using some sort of neutron monochromator and at pulsed neutron imaging facilities by using Time of Flight (TOF) technique. The latter has the highest energy resolution of ΔE/E ~0.2% enabling many in-situ non-destructive studies. It is this type of non-destructive investigations, where MCP/Timepix detector provides many unique experimental capabilities compared to many other types of detection devices. The possibility to time tag every neutron relative to external trigger is used here to calculate the energy of each neutron from the time it traveled from the source to the detector. The combination of a short-pulsed bright neutron beam and a time resolving neutron counting detector enables high resolution energy-resolved imaging experiments to be conducted at the modern spallation neutron sources. There are only few of them available in the world at the present time, limiting the use of this imaging modality to a small number of experiments conducted in a year. However, the unique studies possible only in such experiments make it very attractive for certain applications, some of which are demonstrated in this section.

The schematic representation of an energy-resolved neutron imaging setup is shown in Fig. 9 a (Tremsin et al., 2017a). A short pulse of neutrons is produced by the process of spallation originated by ~100 ns proton pulses produced at 20–60 Hz frequency. The pulse containing neutrons of a wide range of energies produced simultaneously at the spallation source (coupled to a particular neutron moderator) travel towards the detector positioned usually at a distance of ~8–50 m. A large set of energy-resolved images is acquired in one experiment, each corresponding to a particular narrow energy range. Our current MCP/Timepix detector with 512 × 512 pixels acquires thousands of images, thus producing ~250,000 transmission neutron spectra in one experiment. The uniqueness of this experimental setup is also in the fact that a broad range of neutron energies, spanning from ~1 meV cold neutrons to epithermal neutrons exceeding 10 keV energy is measured simultaneously, providing neutron counting detector can resolve time of arrival and position of every neutron with a sufficient accuracy. The analysis of measured transmission spectra allows investigation of various properties of the sample. Thus the variation of transmission in thermal and the cold part of spectrum reveals crystallographic properties due to Bragg scattering occurring for crystalline materials at wavelengths comparable to the spacing between variable lattice plains within the sample (Section 2.2.3.2). The measured transmission in epithermal energy range can be used for the reconstruction of elemental and isotopic composition of the sample as well as for mapping its temperature distribution, both from the analysis of resonance absorption spectra in the epithermal range of energies (see details in Section

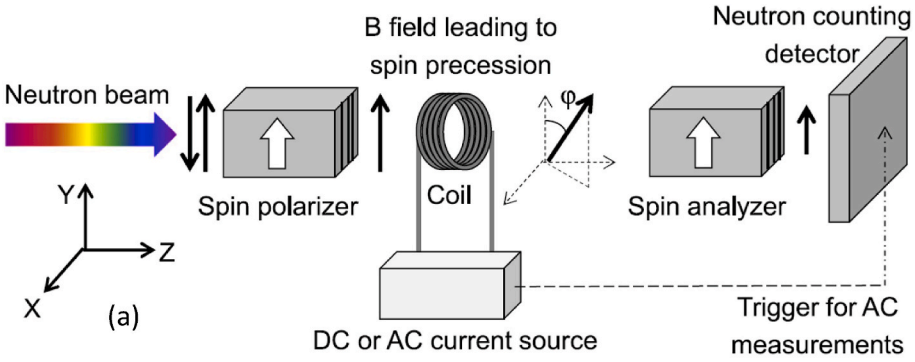

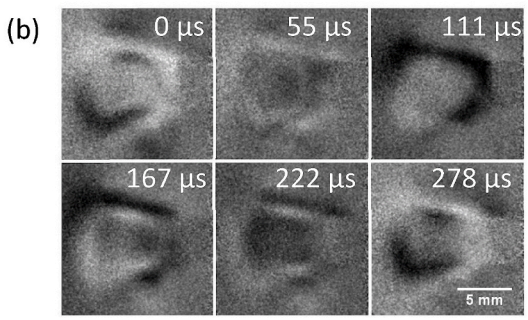

Fig. 7. (a) Schematic diagram of the experimental setup for imaging magnetic fields through neutron spin precession. A sample (coil powered by a current source) is installed between spin polarized and spin analyzer. Neutron counting detector is synchronized with the current source. Time and position of each neutron is detected allowing imaging of dynamic magnetic fields. (b) Spin-polarized neutron radiographs measured for different phases of a dynamic magnetic field. The field is produced by a 15-loop coil with a 3 kHz AC current with 2 A peak-to-peak amplitude. Each image here represents a 10 μs-wide time slice of the AC cycle, indicated by the legend. All phases of the dynamic magnetic field are imaged simultaneously (Tremsin et al., 2015e).

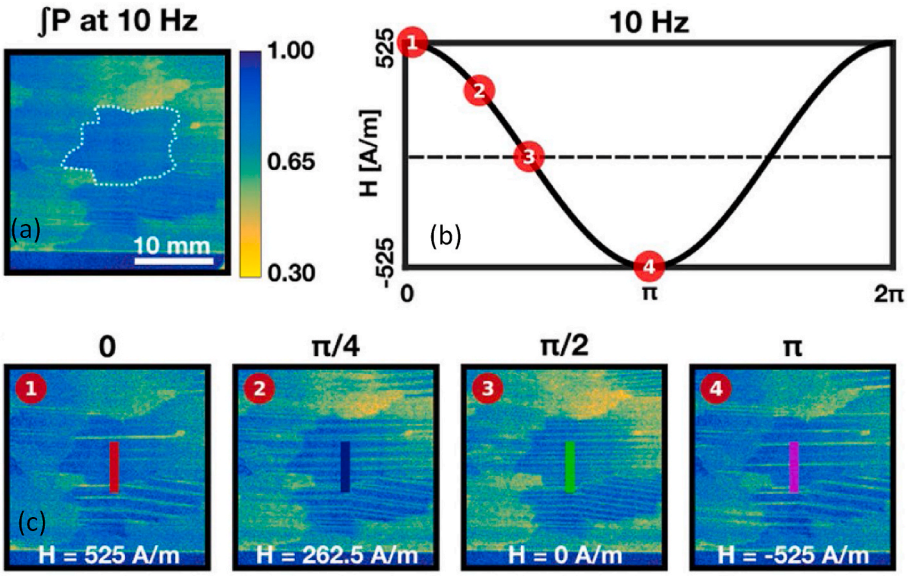

Fig. 8. Neutron dark field images of mobile magnetic domains measured within grain-oriented electrical steel (270 μm thick) covered by an isolation layer. (a) Image of the sample integrated over all phases of 10 Hz power cycle at ±525 A/m. (b) Schematic of the applied sinusoidal field varied at 10 Hz. Red dots indicate the phase of the cycle for which the time-resolved images are shown in (c) (Harti et al., 2018). (For interpretation of the references to color in this figure legend, the reader is referred to the Web version of this article.)

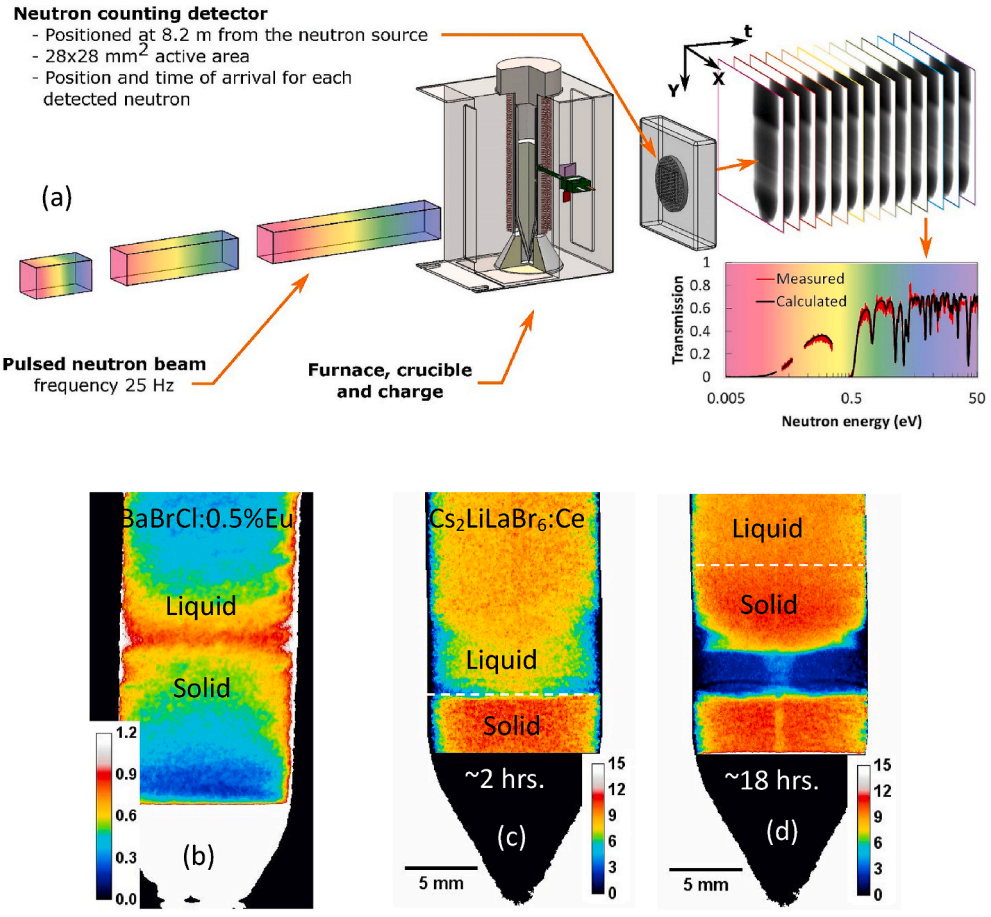

Fig. 9. (a) Schematic diagram of the experimental setup for in-situ diagnostics of crystal growth. A furnace with a charge is installed a few centimeters in front of the detector. A set of images, spanning neutron energies from epithermal range (1–100 eV) to cold neutrons of meV energies is acquired in one experiment. (b) In-situ map of Eu concentration reconstructed from neutron transmission spectra of BaBrCl:0.5%Eu measured during crystal growth (Tremsin et al., 2017a). The color scale indicates Eu concentration in mole %. The interface shape and location are clearly seen in the map due to segregation of Eu. (c), (d) Concentration of Li measured within $Cs_2LiLaBr_6$:Ce charge in-situ at the beginning and the end of crystal growth experiment. The horizontal dashed lines indicate the location of solid/liquid interface. The color bars indicate the atom % concentration of Li within the sample. A very clear band of substantial Li deficiency is seen in (c), which was formed by phase separation (Tremsin et al., 2017b). (For interpretation of the references to color in this figure legend, the reader is referred to the Web version of this article.)

2.2.3.3).

2.2.3.1. In-situ diagnostics of crystal growth. One of the novel capabilities enabled by MCP/Timepix counting detector is the possibility to provide in-situ diagnostics of crystal growth process, which in many cases is limited to indirect measurements of process parameters. That makes the development and optimization of crystal growth recipe very lengthy and expensive for new materials. In many cases, single crystals of relatively large sizes (at least ~1–5 cm in diameter) are required for an efficient device operation (e.g. for the detection of gamma photons and neutron in scintillation detectors). Development of a recipe for the Bridgman growth process, for example (Bridgman, 1925), in many cases is conducted by a trial and error approach, with very limited diagnostics during growth of highly reactive, hygroscopic materials sealed in a

vacuum container. Our neutron imaging experiments with MCP/Timepix detector demonstrated the power of energy-resolved neutron imaging in obtaining multiple process parameters, such as the location and the shape of the interface between liquid and solid phases, maps of elemental composition, the distribution of different phases of the material, formation of defects and the diffusion of certain elements both within the liquid and solid phases (Tremsin et al., 2016a), (Tremsin et al., 2017b). Fig. 9 b shows the elemental map of Eu distribution within BaBrCl:0.5%Eu charge during the crystal growth process. The map of Eu concentration can be reconstructed with up to 0.01% accuracy in that material. Fig. 9c and 9.d demonstrate the capability of neutron imaging to quantify the formation of two separate phases within the melt during the growth of $Cs_2LiLaBr_6$:Ce gamma and neutron scintillator crystal. The accurate map of Li concentration is reconstructed from the measured neutron transmission spectra. MCP/Timepix detectors are used for the investigation of the possibility to optimize crystal growth parameters of multiple novel scintillating and semiconductor materials for the efficient detection of gamma and neutron radiation with high energy and timing resolution. In combination with process simulation, in-situ diagnostics should allow real-time control of crystal growth conditions aiming at improving the quality of grown materials and process yield. Obviously, the industrial growth of crystals will not be implemented in the neutron beamline facilities, but the recipe for the optimal growth conditions can be developed through in-situ imaging and then transferred to the industrial scale production.

2.2.3.2. Engineering applications. Neutron scattering techniques have been widely used for the studies of engineering materials, in particular their crystallographic characteristics such as texture, strain and phase distributions in various metal samples, where neutron penetration provides unique capabilities for non-destructive investigation. Neutron imaging can provide complementary information by mapping crystallographic properties over a relatively large area with high spatial resolution, as opposite to point-by-point scanning implemented in diffraction experiments. The analysis of neutron transmission spectra can be used for the reconstruction of residual strain values (Tremsin et al., 2011b, 2012b, 2014a, 2016b, 2016c, 2018b; Strobl et al., 2012; Woracek et al., 2013; Li et al., 2014; Kirkwood et al., 2015, 2017; Makowska et al., 2016; Wensrich et al., 2016; Hendriks et al., 2017; Gregg et al., 2018; Ramadhan et al., 2018; Sun et al., 2018), distribution of different phases of materials (Kabra et al., 2016), (Song et al., 2017), uniformity of texture (Santisteban et al., 2012), (Dehoff et al., 2015), (Tremsin et al., 2016d), composition of alloying elements (Khong et al., 2016), mapping grains orientation in 3 dimensions (Cereser et al., 2017) and others (Tremsin et al., 2009, 2010c, 2011c, 2016e; Sato et al., 2015; Makowska et al., 2015), as it was demonstrated in recent experiments. Detectors with microchannel plates and Timepix readout enabled the studies of mentioned crystallographic properties with spatial resolution as fine as ~100 μm, limited previously to several millimeters by the capabilities of other neutron counting detectors. Our initial energy-resolved imaging experiments were conducted in conjunction with a well-established neutron diffraction techniques (Tremsin et al., 2012b), as well as several other non-neutron based methods (Ramadhan et al., 2018), (Sun et al., 2018). These experiments proved that the reconstructed stain values, quantitatively agree with the results of other methods (with the limitation of an integral value measured through the sample thickness). In this section we demonstrate a few examples where energy-resolved neutron imaging with MCP/Timeipx detectors was implemented for the non-destructive characterization of engineering materials.

Mapping of strain within the bulk of metal samples has been demonstrated for the residual strain in processed samples, such as welds and additively manufactured specimens (Li et al., 2014), (Tremsin et al., 2016c), (Tremsin et al., 2018b), (Ramadhan et al., 2018), (Santisteban et al., 2012), (Tremsin et al., 2016d), as well as for in-situ loaded samples, such as torqued bolts shown in Fig. 10 (Tremsin et al., 2016b). In this example, the difference in the distribution of strain values is observed for two types of threads, used for the mechanical assemblies. A novel Spiralock® thread appears to be much better suited to vibrational loads due to a larger fraction of bolt being under the load, compared to a regular threaded assembly where only first ~3 threads hold the assembly in place. The uniqueness of this measurement is in the fact that strain distribution in a steel bolt within a steel assembly was mapped with sub-mm resolution in one measurement. Another example of MCP/Timpepix imaging for engineering materials is shown in Fig. 11, where bulk structure and strain distribution are imaged for dissimilar welds, where steel was welded from one side to the underlying Al substrate by application of heat at its front surface (Tremsin et al., 2016c). These results can be used for the proper selection of welding parameters as heat affected zones and strain distribution both in steel and Al parts of the weld can be visualized for the bulk of the sample, compared to excellent studies with other techniques (such as Electron Backscatter Diffraction, EBSD) which are limited to the surface only. Distribution and size of grains within a regular pipe weld can be also visualized from the results of our imaging experiments, as shown in Fig. 12 (Tremsin et al., 2016d), as well as reported in reference (Sun et al., 2018) for friction stir welding Al samples.

It is well known that the advances in additive manufacturing technology enable "3D" printing of very intricate metal structures, which cannot be produced by a conventional manufacturing technology. In addition to complicated geometrical shapes, additive manufacturing allows a very accurate control of grain orientation and structure, which can be used to engineer components where crack propagation, for example, can be diverted away from critical areas. Experiments at Oak Ridge National Laboratory have demonstrated the possibility to print Inconel sample with a designed crystallographic grain orientation, Fig. 13 (Dehoff et al., 2015). EBSD results confirmed the spatial distribution of grain orientation mapped by neutron imaging, except EBSD could only probe the surface, while our energy-resolved neutron imaging visualized the three types of grain orientation all through the bulk of Inconel sample. Several other studies of engineering materials, including 3-dimensional mapping of strain tensor from neutron transmission data, which has been demonstrated recently (Wensrich et al., 2016), (Hendriks et al., 2017), (Gregg et al., 2018), and also in-situ phase transformation (Song et al., 2017) have been conducted with the MCP/Timepix detector as reported in the literature.

2.2.3.3. Elemental-sensitive imaging through resonance absorption. Among the new detector capabilities introduced by the MCP/Timepix devices was the possibility to time tag every neutron with high precision without any afterpulsing (e.g. afterglow in scintillator-based detectors) and at high event rates without readout noise. The very first experiments where epithermal neutrons were imaged with sub-100 ns timing resolution demonstrated that neutron resonance absorption imaging can be performed with ~100 μm spatial resolution, not achievable by other devices at that time. The existence of a distinct set of resonance energies characteristic to a specific element (in fact to an isotope of an element) has been already used for the element-specific imaging at spallation neutron sources, but with very limited spatial resolution (e.g. 10 × 10 pixels) (Perelli Cippo et al., 2011). Despite the fact that the efficiency of current neutron sensitive MCPs is less than 10% in the epithermal range of energies, as it drops rapidly with the increase of neutron energy (defined by ^{10}B absorption cross section), sufficiently high flux of epithermal neutrons in the imaging beamlines makes it possible to acquire element-specific images in a reasonable time (typically minutes to hours). In addition to high temporal and spatial resolution, detectors for resonance absorption imaging have to survive in intense gamma and fast neutron radiation fields, as no choppers can be used during such experiments. Choppers are too slow for the epithermal energies, and can only be used for thermal and cold neutron experiments. A large number

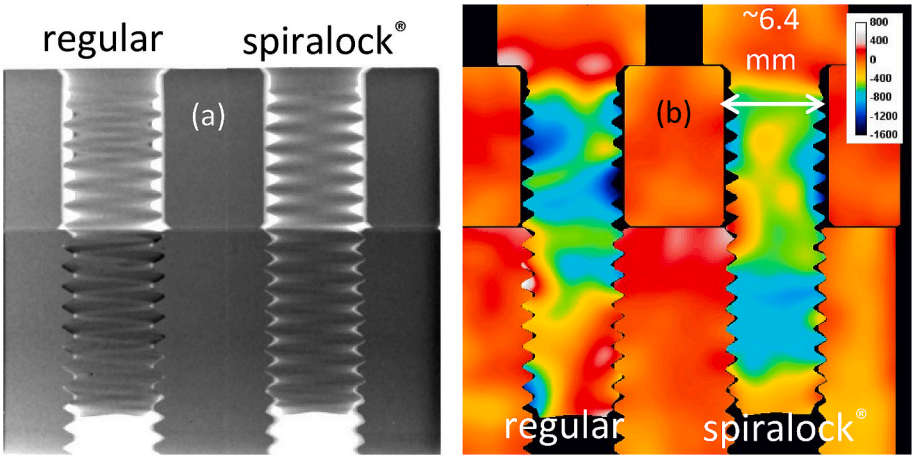

Fig. 10. (a) White spectrum neutron transmission image of steel assembly with torqued steel bolts. A regular thread and a specially designed for vibrational stability Spiralock® thread are implemented in the assembly. (b) Strain maps across the steel assembly with torqued bolts reconstructed from energy-resolved images by the analysis of transmission spectra around each 55 μm pixel. The strain values are integrated through the thickness of the sample. The legend indicates the color bar for measured strain values in microstrain (Tremsin et al., 2016b). (For interpretation of the references to color in this figure legend, the reader is referred to the Web version of this article.)

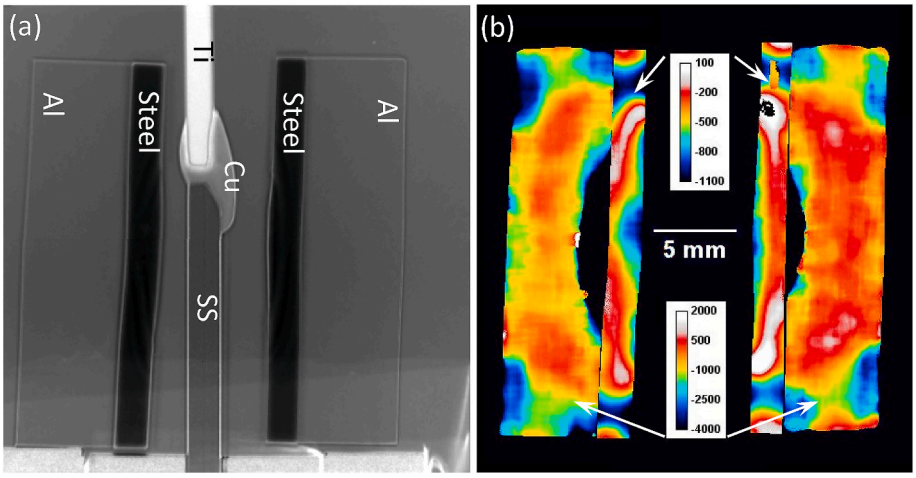

Fig. 11. (a) Neutron transmission image of three dissimilar weld samples: Ti to stainless steel with copper filler (middle weld) and Al to steel (left and right samples). Image integrated over the neutron wavelengths 1–4.16 Å was normalized by the image obtained past the last Bragg edge (4.18–8 Å). (b) Residual strain map of Al/Steel dissimilar welds reconstructed from energy-resolved imaging (Tremsin et al., 2016c).

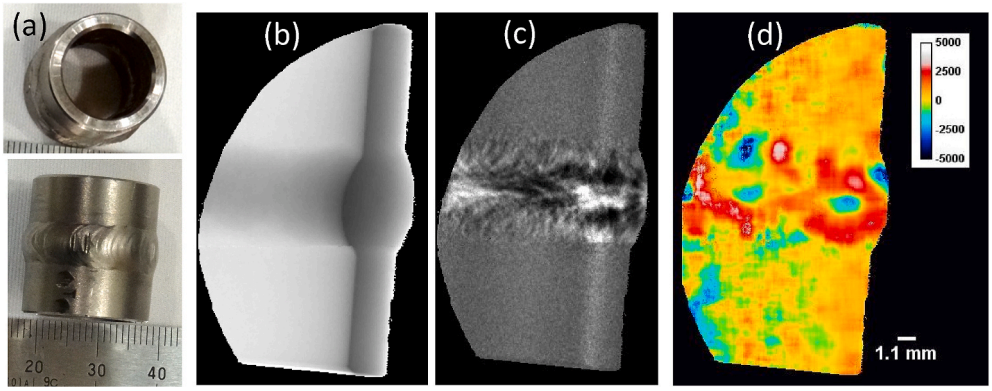

Fig. 12. (a) Photograph of the steel pipe weld imaged in the experiment. (b) White spectrum neutron radiography showing the variation of thickness of the material along the neutron path. (c) Narrow-wavelength neutron transmission image around 1.96 Å. The distribution of preferred grain orientations in the weld area is seen in that image. (d) Residual strain map reconstructed from measured transmission spectra around (111) Bragg edge (Tremsin et al., 2016d).

of gamma photons are produced at the time of spallation, as well as fast neutrons, which reach the detector within first few microseconds after spallation. These events can overwhelm the detector, which needs to recover and measure incoming neutrons as early as ~10 μs after the spallation. MCP/Timepix devices demonstrated excellent stability in high radiation environment (Tremsin et al., 2018c), (Tremsin et al., 2019b) and were capable of measuring transmission neutron spectra with good accuracy up to ~30 keV energies (Tremsin et al., 2014b). Not all elements have resonance energies below that ~30 keV threshold, limiting resonance absorption imaging to those elements/isotopes,

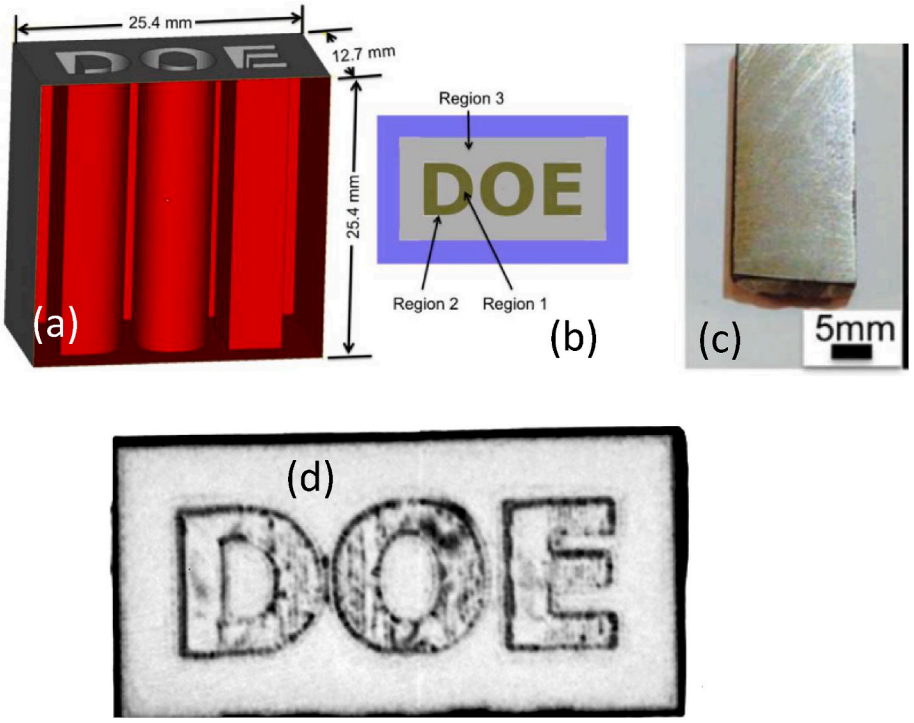

Fig. 13. (a) Schematic diagram of the Inconel 718 sample printed by an additive manufacturing technique with electron beam melting. Three different crystallographic grain orientation regions are printed within the sample. (b) Region 1: mixed mode that is combination of columnar and equiaxed growth; Region 2: highly misoriented equiaxed grain growth; Region 3: 001. columnar grain growth. (c) Photograph of 5 mm-thick sample cut out of the larger printed specimen. (d) Narrow-energy neutron transmission image of the sample visualizing the difference in grain orientation between 3 regions. The contrast in the image caused by neutron diffraction appearing at this wavelength for the grains predominantly in regions 1 and partially in region 2 (Dehoff et al., 2015).

which have sufficiently high absorption cross section in ~0.1–1000 eV range. It is important to emphasize here that resonance element-specific imaging in the epithermal range and imaging of crystallographic characteristics in the thermal and cold ranges can be performed simultaneously with MCP/Timepix detectors, all in one measurement at a spallation neutron source, with no need to scan through the energies (Tremsin et al., 2012c, 2013c, 2015f, 2017c, 2017d; Ooi et al., 2013).

An example of where neutron resonance absorption imaging provides a unique non-destructive investigation of bulk characteristics was demonstrated in the investigation of single-crystal and polycrystalline gold samples, as shown in Fig. 14 (Tremsin et al., 2017d). To the best of our knowledge, there are presently no non-destructive techniques which

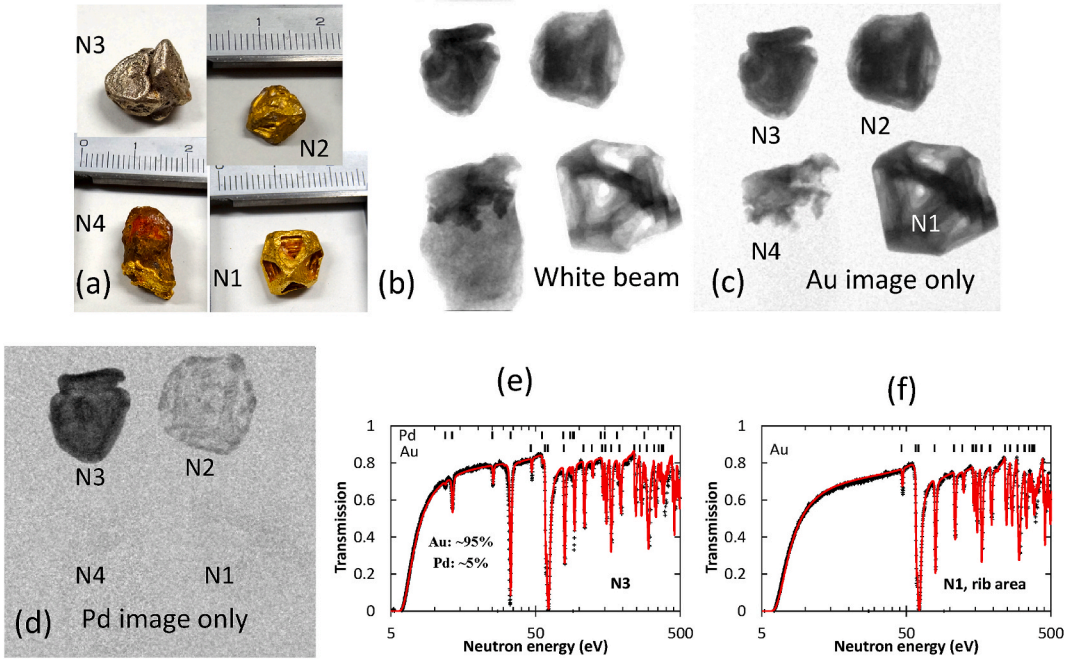

Fig. 14. (a) Photograph of four naturally grown gold samples studied in the experiment. (b) White spectrum neutron transmission image of gold samples acquired with an MCP/Timepix detector. (c) A narrow-energy neutron transmission image where the contrast due to gold resonance absorption is enhanced by selection of specific energies (around 5 eV) and normalized by an image integrated over non-resonant energies. (d) Same as image (c) except integrated over resonance energies of Pd. Distribution of Pd within the bulk of gold sample is imaged. (e), (f) Measured neutron transmission spectra in the epithermal range of energies, demonstrating the presence of sharp absorption features due to Au and Pd (Tremsin et al., 2017d). (For interpretation of the references to color in this figure legend, the reader is referred to the Web version of this article.)

can probe the internal structure of a cm-scale gold sample due to its high opacity. Epithermal neutron, on the other hand, can investigate the internal structure of such a thick gold specimen and reveal the presence of other elements, and even map their distribution within gold. The transmission spectrum of two gold samples shown in Fig. 14e and 13 f have difference in the resonance dips, as sample N3 contained several % of Pd exhibiting resonances at ~13eV, 25eV and the strongest resonance dip at ~33 eV seen in Fig. 14 e. Selecting the images in the energy-resolved stack for the energies where only gold is absorbing results in the exclusive map of gold distribution within the sample, as shown in Fig. 14 c. Images measured around Pd resonance reveal the distribution of Pd within gold, demonstrating the strength of element-specific imaging through resonance absorption, Fig. 14 d. Even gaseous materials encapsulated within high-Z metals can still be visualized by this novel imaging technique, as was demonstrated in an experiment where overlapping steel containers containing UO_2, Gd, W and Xe gas were imaged with an MCP/Timepix detector (Tremsin et al., 2017c), Fig. 15. All these elements were imaged virtually independently from each other by selection of corresponding range of neutron energies, highlighted in the spectra shown in Fig. 15, except for the steel, which was imaged indirectly by the molybdenum included in steel, as iron does not have resonance in the accessible range of energies. In addition to elemental analysis, it has also been demonstrated that Doppler broadening of neutron resonance can be used to remotely measure temperature. Very accurate measurements performed previously with a single-pixel devices (Yuan et al., 2005), (Schillebeeckx et al., 2012) has been extended to a spatially-resolved map of temperature distribution reconstructed from the data measured with an MCP/Timepix detector (Tremsin et al., 2015f) with sub-mm spatial resolution.

2.2.3.4. Cultural heritage and unique samples: non-destructive studies by neutron imaging. Neutron imaging has been shown to be a very attractive technique for the studies of various unique or rate specimens, where non-destructiveness is absolutely crucial, such as in the studies of museum or cultural heritage objects, rare samples as meteorites, and others. It should be noted here, that in addition to relatively high penetration of neutrons into objects opaque to other types of radiation, there is a possibility of sample activation through neutron absorption reaction, which can create a radioactive isotope. A careful experiment planning, as well as prompt gamma activation analysis can be employed before conduction of neutron imaging on a particular precious sample. If activated material has a short life time, a cool-down period can be implemented before the sample is released from the imaging facility. Another consideration to be taken here is the limited number of relevant facilities. The energy-resolved neutron imaging experiments can only be conducted currently at large facilities, namely spallation neutron or reactor-based sources, where samples have to be transported to, not within the museums or other places of storage of those objects. However, the uniqueness of non-destructive study of the internal structure of a particular specimen make neutron imaging still very attractive for the studies of certain objects (Barzagli et al., 2014), (Kiyanagi et al., 2015). Recently a substantial interest was raised to the investigation of the internal structure of various Japanese swords, which have different crystallographic characteristic depending on a particular manufacturer and a time period. The detailed knowledge on the internal structure of a particular sword may be used to uncover and to correlate various sword manufacturing techniques used in the distant past and lost due to the tradition to keep them secret. An example of such imaging experiment is shown in Fig. 16, where the interface between the core and the exterior metals can be clearly visualized by neutron imaging, as well as single crystal inclusions produced at the interface between two components of a sword during cold working. Neutron imaging of other unique or expensive objects, such as gems, for example, was also conducted with an MCP/Timepix detector recently, where a cultivated pearl could be reliably distinguished from a natural specimen (Vitucci et al., 2018). Studies of metallic meteorites can be another attractive area of applications of MCP/Timepix neutron imaging detectors as the bulk structure of the sample can be investigated non-destructively for the presence of preferred grain orientation, as demonstrated in Fig. 17 (Tremsin et al., 2019). The meteorite in that study was sliced, revealing the presence of textured features within the bulk, not visible on the surface, while neuron imaging can provide that information non-destructively.

2.3. Applications in mass spectroscopy, biology and others

A combination of an MCP electron multiplier and Timepix readout was a crucial component in the successfully implemented time of flight mass spectrometry imaging, Fig. 18, at FOM Institute for Atomic and Molecular Physics (AMOLF) and National Institute for Subatomic Physics (Nikhef), both in Netherlands (Jungmann et al., 2011), (Jungmann et al., 2012), (Jungmann et al., 2013). Acquisition of time resolved images of several m/z species was made possible by the fast Timepix readout in a single measurement, which was limited only by timing resolution of Timepix readout (10 ns for that first generation of Timepix chips). The results of these experiments have demonstrated that a mass range up to 100 kDa is accessible with such detection system (Jungmann et al., 2013).

Another experimental setup where both microchannel plate amplifiers and a Timeipx-based readout were implemented was built for the coincidence velocity map imaging, Fig. 19 (Zhao et al., 2017). Different from the previously reposted MCP amplifiers coupled directly to a set of bare Timepix chips in vacuum, in these experiments there were additional signal conversions implemented between the MCPs and the Timepix readout. The incoming particles (both ions and electrons) were initially registered by a set of microchannel plates in vacuum and amplified with the gain of $\sim 10^6$. The output charge impinged on a phosphor screen, producing splashes of visible photons at the air side of the vacuum vessel. These light clusters on the phosphor screen were imaged by a Tpx3Cam – a time stamping optical camera with 1.5 ns timing resolution, positioned outside of vacuum vessel. The authors indicate that such setup can be useful for a wide range of experiments that produce electrons and ions whose momenta yield important information about molecular structure and dynamics, such as studies of reaction dynamics and strong field laser-matter interactions (Zhao et al., 2017). The Tpx3Cam was a subsequent development of TimepixCam reported in references (Fisher-Levine and Nomerotski, 2016), (Nomerotski et al., 2017), which was originally used for the velocity-map imaging experiments at a free electron laser (Fisher-Levine et al., 2018).

A directly coupled MCP amplifier to a quad Timepix readout was used in another experimental setup for ion-ion coincidence measurements with repeller, extractor and ground electrodes (Long et al., 2017). The high ~50 ps time resolution in this setup was achieved by combining the MCP output signal digitized by a Time to Digital Converter with the spatial information provided by the Timepix readout with sub-pixel event centroiding. Synchronization of timing and positional channels is quite challenging in such setup and it limits the rate of incoming particles to $\sim 10^5$ Hz, above which it is very difficult to reliably correlate the spatial and timing channels.

Application of the TimepixCam for phosphorescence lifetime imaging experiments demonstrated the capabilities of photon counting systems with Timepix readout to measure lifetime curves in a large number of pixels, all simultaneously (Michalet et al., 1611), (Hirvonen et al., 2017). Fig. 20 shows a color-mapped image of iridium bids with different phosphorescence life time with exponential constants on the scale of ~0.5 ns, which is too slow compared to fluorescence lifetime of dyes used in biological imaging. The measured difference in the lifetime between different iridium compounds allows identification of bids iridium composition, although the lifetime of the fluorescent plastic (which is on the order of a few nanoseconds) was too short for the present experimental setup. Although these experiments were conducted with timing resolution of ~15 ns limited by the Timeipx readout

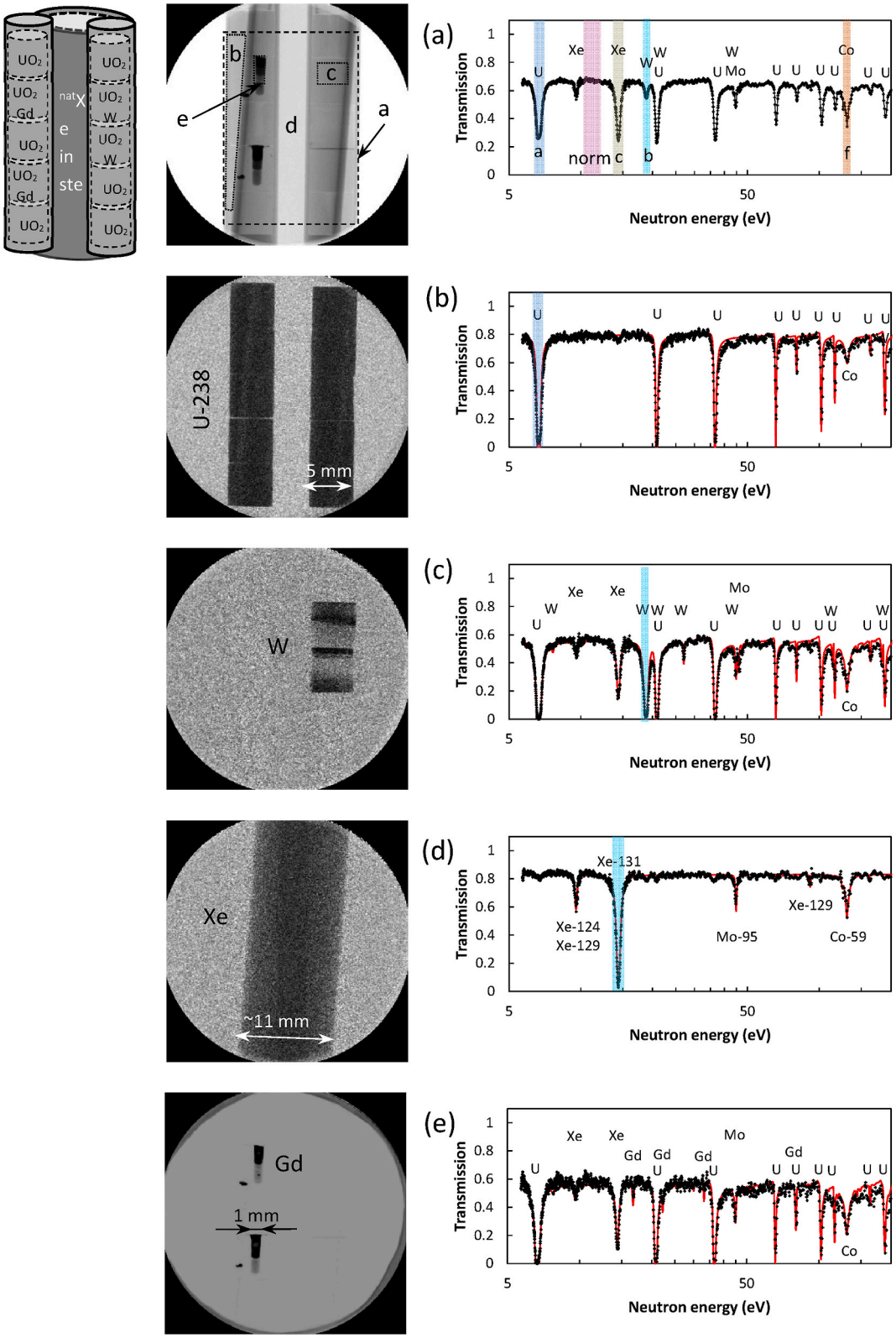

Fig. 15. Element-specific images acquired with overlapping samples positioned in front of each other as schematically shown at the top diagram. (a) Full spectrum (white beam) radiograph and a spectrum obtained in the area indicated by a wide dashed rectangle. The letters in the radiograph indicate the areas for which spectra are extracted in figures (b)–(e). The energy ranges shown by the shaded areas in the spectrum of figure (a) indicate the energy range for the subset of images which were used to reconstruct the element-specific maps (b)–(e), except for the map of Gd, where thermal neutrons were used due to high absorption cross section of Gd. ^{238}U, W, Xe and Gd are imaged separately from other elements despite the fact they were overlapped with each other as well as with steel pipes (Tremsin et al., 2017c).

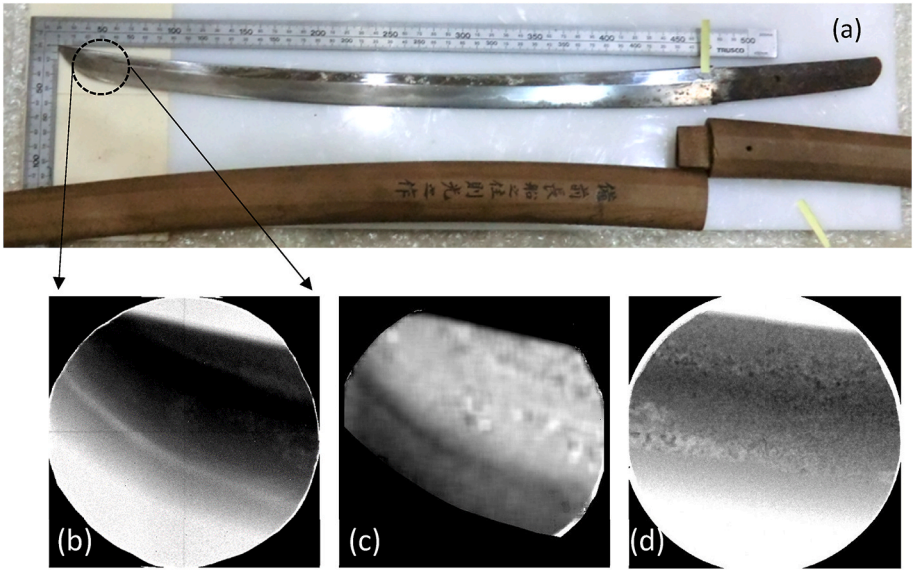

Fig. 16. (a) Photograph of an ancient Japanese sword imaged in the experiment. The area of the tip where images (b)–(d) are measured is shown by a dashed circle. (b) Neutron transmission image integrated at wavelengths ~1–4 Å (before the last Bragg edge) divided by the image acquired over wavelengths ~4.5–8 Å (past the last Bragg edge). A distinct line between two metal sword components is clearly seen. (c) The fitted value of Bragg edge height emphasizing the difference between two steels used during sword manufacturing. (d) Narrow-energy neutron transmission image showing the presence of individual large grains which formed during sword manufacturing process in between two steel components.

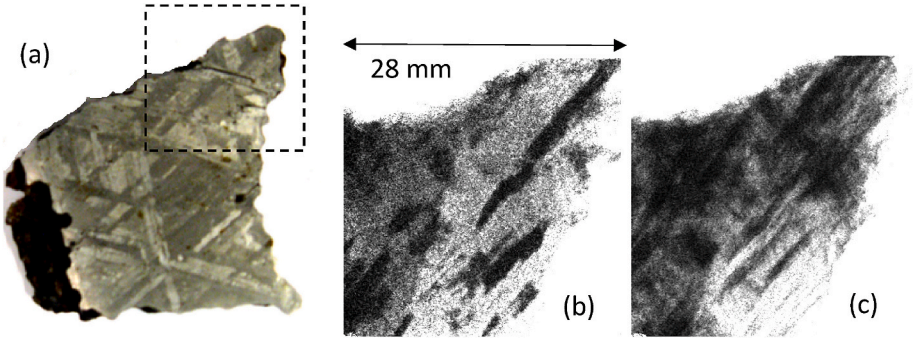

Fig. 17. (a) Photograph of a metallic meteorite, which was cut to visualize the internal texture distribution. Dashed rectangle shows the area imaged with neutrons. (b), (c) Narrow-energy neutron transmission images revealing the presence of preferred grain orientation in the bulk of the crystal. Neutron diffraction by grains with similar orientation reduces the intensity of transmitted image in corresponding areas. The internal crystallographic structure of meteorite can be mapped non-destructively by neutron imaging.

(which is improved by an order of magnitude in Tpx3Cam), these results indicate that with introduction of Timepix4 chips with the timing resolution of ~0.2 ns the detectors with MCP amplifiers and Timeix readout can be attractive for future lifetime imaging applications. For the highest resolution for the lifetime curves, may be a combination of MCP amplifier with a bare Timepix4 readout in a vacuum tube with a visible photocthode will be best option in order to avoid the contribution of the phosphor decay time.

3. Near future improvements of MCP/Timepix detectors

The majority of the results reported in this paper were obtained with a microchannel plate detector coupled to a quad Timepix readout, with few exceptions reported in Section 2.3, where more advanced Timepix3 readout was used coupled to a Si sensor registering photons produced by an MCP image intensifier. The ongoing development in the University of California at Berkeley to build an MCP detector directly coupled in vacuum to Timepix3 readout promises to bring new capabilities to neutron counting detectors by enabling simultaneous detection of time of arrival and charge for each registered neutron at rates exceeding 40 MHits/sec/cm^2. That should allow measurement of neutron transmission spectra in energy resolved imaging experiments with no readout gaps (320 μs readout dead time presently). In addition, high spatial resolution to ~10 μm level through the event centroiding will be possible for the energy-resolved neutron imaging experiments limited currently to 55 μm pixel size.

A substantial interest in MCP/Timepix detectors was also raised by the synchrotron and free electron laser (FEL) community for soft X-ray detection in applications ranging from inelastic X-ray scattering, to photon correlation spectroscopy and others. Simultaneous detection of multiple X-ray photons, converted to a photoelectron and then amplified by an MCP stack, with timing resolution of ~1.6 ns will be possible with such devices with no readout noise and at high input rates. The upgraded LCLS-II at Stanford University, California, which will be operating at ~ Mhz repetition rates will benefit from the capability of MCP/Timepix detector to associate each registered photon to the original X-ray pulse, needed for the advanced pump-probe FEL experiments.

In the longer term, the expected development of Timepix4 will substantially extend the capabilities of MCP/Timepix detectors to larger formats, higher timing resolution and higher counting rates. The through silicon vias (TSVs) of Timepix4 readout will make these chips buttable on all 4 sides, which is crucial for large area MCP detectors. While our colleagues marvelously managed to make seamless 10 × 10 cm^2 Timepix detectors by tilting the underlying back-thinned Timepix chips (Jakubek et al., 2014), that is not an option for the bare chip readout used in MCP detectors. Tiling Timepix to a 10 × 10 cm^2 format in vacuum MCP detectors will be very attractive for the neutron imaging applications and for the future NASA large area telescopes, where detectors as large as 20 × 20 cm^2 will be needed in the focal plane to match the performance of the telescope optics. Biological imaging applications, such as Fluorescence Lifetime Imaging and Förster Resonance Energy Transfer will greatly benefit from the development of MCP/Timepix4 detectors, where timing resolution of ~0.2 ns will match the requirements of lifetime curves with time constants of few nanoseconds. Simultaneous detection of a large array of cells, as well as imaging of a live cell migrating within the focal spot will be enabled by such detector

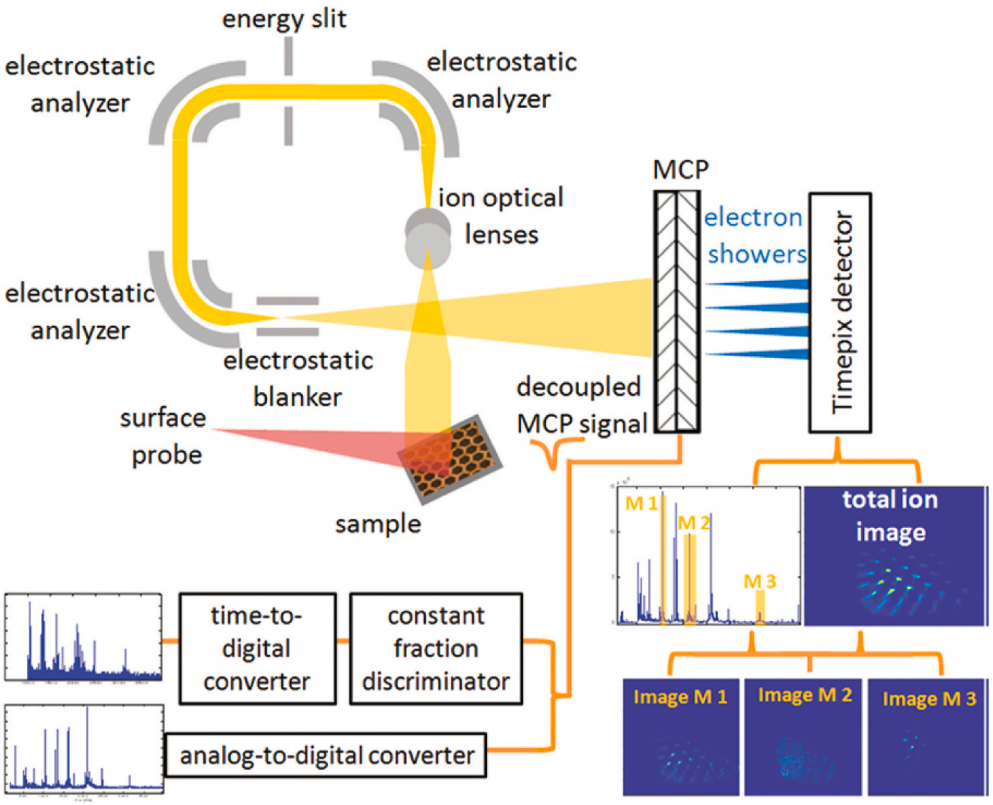

Fig. 18. Schematic representation of Mass Spectrometry Imaging setup, where MCP/Timeipx detector enabled time resolved mass spectrometry with a substantially increased dynamic range. An MCP-Timepix detector assembly was coupled to an ion microscope, enabling simultaneous detection of mass spectra, total and mass-selected ion images without the need for mass selection and repetitive measurements (Jungmann et al., 2011).

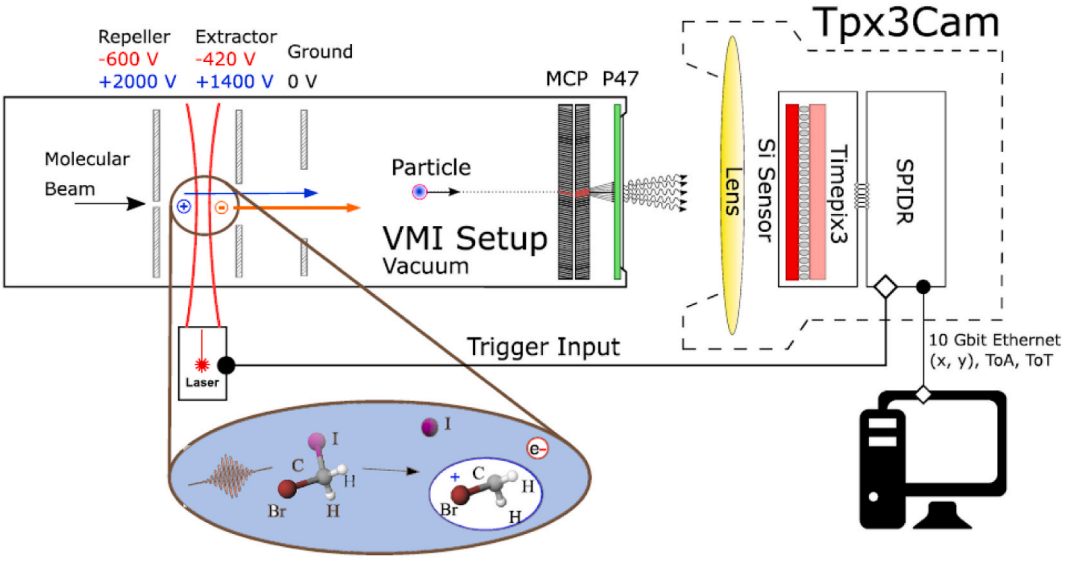

Fig. 19. Schematic diagram of an experimental setup for coincidence velocity map imaging (VMI) experiments, where and MCP is used in vacuum to convert incoming particles into the visible light upon collision of output electrons with a phosphor screen. The photons produced by the phosphor screen then encoded by a fast Timepix3-based camera mounted outside of vacuum chamber. The laser beam intersects an effusive molecular beam (e.g., CH_2IBr) between repeller and extractor plates, producing photoelectrons and photoions (CH_2Br^+). The voltages on the VMI plates are switched from negative to positive immediately after the electrons leave the accelerating region. Due to the large difference in mass, both electrons and ions are projected onto the dual stack of MCPs, producing $\sim 10^6$ electrons for each incident particle. The position (x,y), time of arrival (ToA) and total charge (proportional to the number of electrons hitting the phosphor screen) are registered for each particle by a Tpx3Cam sensor (Zhao et al., 2017).

with its large number of pixels compared to currently used Single Photon Avalanche Diode arrays.

At the same time, there will be other new applications of event counting MCP/Timepix detectors in some unconventional areas which are hard to envision at the present time. When MCP detectors were developed originally for low light level applications, it was hard to

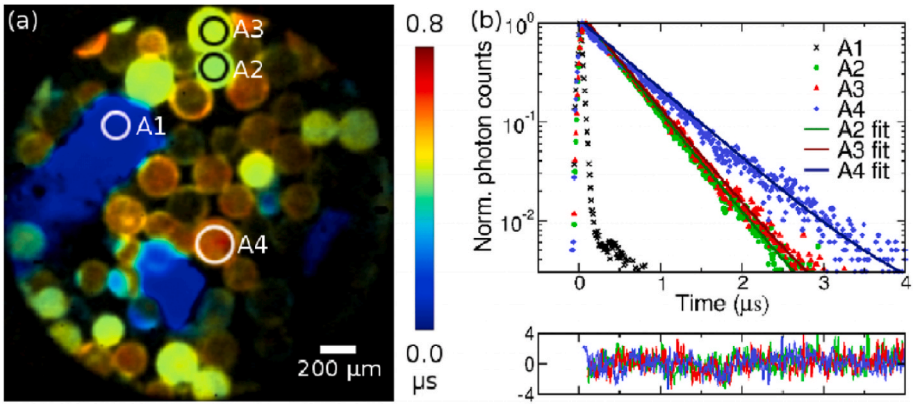

Fig. 20. (a) Lifetime images of beads infused with different Ir-compounds and fluorescent plastic acquired with TimepixCam. (b) Intensity as a function of time (phosphorescence decays) for areas A1-A4 indicated in (a), with monoexponential fits to the phosphorescence decays and residuals of the fits. The lifetime of fluorescent plastic was too short for the setup based on Timepix readout with its limited ~15 ns timing resolution. Future Timeipx4 readout with ~0.2 ns should enable lifetime imaging with much shorter decay constants (Hirvonen et al., 2017).

predict that they will be used in imaging with incoming fluxes reaching GHz event rates, with many simultaneously arriving particles in such diverse areas as reported in this paper. It is the pixelated readout Medipix/Timepix technology which revolutionized certain aspects of MCP detection technology, substantially extending the areas of their applications. We are looking forward to new developments within the very collaborative and open environment within the Medipix collaboration led by our colleagues at CERN.

Acknowledgements

The MCP/Timepix detector used in the experiments described in the this paper was developed in the University of California at Berkeley in collaboration with Nova Scientific Inc. Sturbridge, MA, USA, the manufacturer of neutron sensitive microchannel plates and Techne instruments, Oakland, CA, USA with great help from the Medipix collaboration, in particular with help of our colleagues from Advacam with the development and manufacturing of Timepix readout boards, the Institute of Experimental and Applied Physics, Czech Technical University in Prague who shared their open-architecture Pixelman data acquisition software (Turecek et al., 2011) enabling custom hardware plugins, NiKHEF helping us with their advice on the Timepix assemblies and readout electronics and the entire team of Medipix/Timepix chip designers at CERN with their invaluable advice on the Timepix readout. The results presented in this review were obtained with a great help and in collaboration with many scientists and engineers working at various neutron imaging facilities and with many colleagues from various Universities, National Laboratories and industry, all of whom are listed as co-authors in the references in this manuscript. Their advice, enthusiasm, scientific, technical and moral support were invaluable during the development of MCP/Timepix detector and its applications in various imaging experiments. We express many thanks for the granted access to nearly all neutron imaging user facilities around the world. The work on the MCP/Timepix detector at the University of California was partially funded through the research grants by the United States Department of Energy, National Science Foundation and National Aeronautics and Space Administration.

References

Adams, B.W., Elagin, A., Frisch, H.J., Obaid, R., Oberla, E., Vostrikov, A., Wagner, R.G., Wang, J., Wetstein, M., 2015. Timing characteristics of large area picosecond photodetectors. Nucl. Instrum. Methods Phys. Res. 795, 1–11.

Ballabriga, R., Campbell, Michael, Llopart, Xavier, 2018. Asic developments for radiation imaging applications: the medipix and timepix family. Nucl. Instrum. Methods Phys. Res. A 878, 10–23.

Barzagli, E., Grazzi, F., Salvemini, F., Scherillo, A., Sato, H., Shinohara, T., Kamiyama, T., Kiyanagi, Y., Tremsin, A., Zoppi, Marco, 2014. Wavelength Resolved Neutron Transmission Analysis to identify single crystal particles in historical metallurgy". Eur. Phys. J. Plus 129, 158.

Bellazzini, R., Spandre, G., Minuti, M., Brez, A., Baldini, L., Latronico, L., Omodei, N., Sgro, C., Bregeon, J., Razzano, M., Pinchera, M., Tremsin, A.S., McPhate, J.B., Vallerga, J.V., Siegmund, O.H.W., 2008. Single photon imaging at ultra-high resolution. Nucl. Instrum. Methods A. 591, 125–128.

Bridgman, P.W., 1925. Certain physical properties of single crystals of tungsten, antimony, bismuth, tellurium, cadmium, zinc, and tin. Proc. Am. Acad. Arts Sci. 60, 305.

Buitrago, N.L., Santisteban, J.R., Tartaglione, A., Marín, J., Barrow, L., Daymond, M.R., Schulz, M., Grosse, M., Tremsin, A., Lehmann, E., Kaestner, A., Kelleher, J., Kabra, S., 2018. Determination of very low concentrations of hydrogen in zirconium alloys by neutron imaging. J. Nucl. Mater. 503, 98–109.

Cereser, A., Strobl, M., Hall, S., Steuwer, A., Kiyanagi, R., Tremsin, A.S., Knudsen, E.B., Shinohara, T., Willendrup, P., da Silva Fanta, A.B., Iyengar, S., Larsen, P.M., Hanashima, T., Moyoshi, T., Kadletz, P.M., Krooß, P., Niendorf, T., Sales, M., Schmahl, W.W., Schmidt, S., 2017. Time-of-Flight three dimensional neutron diffraction in transmission mode for mapping crystal grain structures. Sci. Rep. 7, 9561.

Cheng, C.-L., Perfect, E., Donnelly, B., Bilheux, H.Z., Tremsin, A.S., McKay, L.D., Distefano, V.H., Cai, J.C., Santodonato, L.J., 2015. Rapid imbibition of water in fractures within unsaturated sedimentary rock. Adv. Water Resour. 77, 82–89.

Dehoff, R.R., Kirka, M.M., Sames, W.J., Bilheux, H., Tremsin, A.S., Lowe, L.E., Babu, S.S., 2015. Site specific control of crystallographic grain orientation through electron beam additive manufacturing. Mater. Sci. Technol. 31, 931–938.

Fiorini, M., Alozy, J., Bolognesi, M., Campbell, M., Cotta Ramusino, A., LLopart, X., Michel, T., Schifano, S.F., Tremsin, A., Vallerga, J., 2018. Single-photon imaging detector with O(10) ps timing and sub-10 μm position resolutions. J. Instrum.JINST 13, C12005.

Fisher-Levine, M., Nomerotski, A., 2016. TimepixCam: a fast optical imager with time-stamping. J. Inst. Met. 11, C03016.

Fisher-Levine, M., Boll, R., Ziaee, F., Bomme, C., Erk, B., Rompotis, D., Marchenko, T., Nomerotski, A., Rollese, D., 2018. Time-resolved ion imaging at free-electron lasers using TimepixCam. J. Synchrotron Radiat. 25, 336–345.

Fraser, G.W., 1995. Thermal neutron imaging. Proc. SPIE 2339, 287–301.

Fraser, G.W., 2001. Imaging in astrophysics (and elsewhere). Nucl. Instrum. Methods A 471, 170–173.

Gregg, A.W.T., Hendriks, J.N., Wensrich, C.M., Wills, A., Tremsin, A., Luzin, V., Shinohara, T., Kirstein, O., Meylan, M., Kisi, E.H., 2018. Tomographic reconstruction of two-dimensional residual strain fields from bragg-edge neutron imaging. Phys. Review Applied 10, 064034.

Harti, R.P., Strobl, M., Schäfer, R., Kardjilov, N., Tremsin, A.S., Grünzweig, C., 2018. Dynamic volume magnetic domain wall imaging in grain oriented electrical steel at power frequencies with accumulative high-frame rate neutron dark-field imaging. Sci. Rep. 8, 15754.

Hendriks, J.N., Gregg, A.W.T., Wensrich, C.M., Tremsin, A.S., Shinohara, T., Meylan, M., Kisi, E.H., Luzin, V., Kirsten, O., 2017. Bragg-edge elastic strain tomography for in situ systems from energy-resolved neutron transmission imaging. Phys. Rev. Materials 1, 053802.

Hilger, A., Manke, I., Kardjilov, N., Osenberg, M., Markötter, H., Banhart, J., 2018. Tensorial neutron tomography of threedimensional magnetic vector fields in bulk materials. Nature Comunications 9, 4023.

Hirvonen, L.M., Fisher-Levine, M., Suhling, K., Nomerotski, A., 2017. Photon counting phosphorescence lifetime imaging with TimepixCam. Rev. Sci. Instrum. 88, 013104.

Inami, K., Mori, T., Matsumura, T., Kurimoto, K., Hasegawa, S., Suzuki, Y., Murase, T., Yurikusa, Y., Akatsu, M., Enari, Y., Hokuue, T., Tomita, A., Kishimoto, N., Ohshima, T., Ihara, T., Nishizaw, H., 2008. Cross-talk suppressed multi-anode MCP-PMT. Nucl. Instrum. Methods Phys. Res. 592, 247–253.

Jakubek, J., Holy, T., Lehmann, E., Pospisil, S., Uher, J., Vacik, J., Vavrik, D., 2006. Neutron imaging with Medipix-2 chip and a coated sensor. Nucl. Instrum. Methods Phys. Res. 560, 143–147.

Jakubek, J., Jakubek, M., Platkevic, M., Soukup, P., Turecek, D., Sykoraa, V., Vavrik, D., 2014. Large area pixel detector WIDEPIX with full area sensitivity composed of 100 Timepix assemblies with edgeless sensors. J. Inst. Met. 9, C04018.

Jungmann, J.H., MacAleese, L., Visser, J., Vrakking, M.J.J., Heeren, R.M.A., 2011. High dynamic range bio-molecular ion microscopy with the timepix detector. Anal. Chem. 83, 7888–7894.

Jungmann, J.H., Smith, D.F., MacAleese, L., Klinkert, I., Visser, J., Heeren, R.M.A., 2012. Biological tissue imaging with a position and time sensitive pixelated detector. J. Am. Soc. Mass Spectrom. 23, 1679–1688.
Jungmann, J.H., Smith, D.F., Kiss, A., MacAleese, L., Buijs, R., Heeren, R.M.A., 2013. An in-vacuum, pixelated detection system for mass spectrometric analysis and imaging of macromolecules. Int. J. Mass Spectrom. 341– 342, 34– 44.
Just, F., Filipenko, M., Cavanna, A., Michel, T., Gleixner, T., Taheri, M., Vallerga, J., Campbell, M., Tick, T., Anton, G., Chekhova, M.V., Leuchs, G., 2014. Detection of non-classical space-time correlations with a novel type of single-photon camera. Opt. Express 22, 17561.
Kabra, S., Kelleher, J., Kockelmann, W., Tremsin, A.S., 2016. Energy-dispersive neutron imaging and diffraction of magnetically driven twins in a Ni2MnGa single crystal magnetic shape memory alloy. J. Phys. Conf. Ser. 746, 012056.
Kardjilov, N., Manke, I., Strobl, M., Hilger, A., Treimer, W., Meissner, M., Kristi, T., Banhart, J., 2008. Three-dimensional imaging of magnetic fields with polarized neutrons. Nat. Phys. 4, 399–403.
Khong, J.C., Daisenberger, D., Burca, G., Kockelmann, W., Tremsin, A.S., Mi, J., 2016. Design and characterisation of metallic glassy alloys of high neutron shielding capability. Sci. Rep. 6, 36998.
Kirkwood, H.J., Zhang, S.Y., Tremsin, A.S., Li, W., Korsunsky, A., Baimpas, N., Abbey, B., 2015. Neutron strain tomography using the radon transform. Mater. Today: Proceedings 2S, S414–S423.
Kirkwood, H.J., Zhang, S.Y., Tremsin, A.S., Sui, T., Korsunsky, A.M., Abbey, B., 2017. High resolution imaging and analysis of residual elastic strain in an additively manufactured turbine blade. Int. J. Nanotechnol. 14, 166–178.
Kiyanagi, Y., Ayukawa, N., Shiota, Y., Kino, K., Sato, T., Sato, H., Kamiyama, T., Grazzi, F., Scherillo, A., Uno, S., Tremsin, A.S., 2015. Application of a pulsed neutron transmission method to a cultural heritage study. Restaurierung und Archäologie 8, 85–91.
Kockelmann, W., Minniti, T., Pooley, D.E., Burca, G., Ramadhan, R., Akeroyd, F.A., Howells, G.D., Moreton-Smith, C., Keymer, D.P., Kelleher, J., Kabra, S., Lee, T.L., Ziesche, R., Reid, A., Vitucci, G., Gorini, G., Micieli, D., Agostino, R.G., Formoso, V., Aliotta, F., Ponterio, R., Trusso, S., Salvato, G., Vasi, C., Grazzi, F., Watanabe, K., Lee, J.W.L., Tremsin, A.S., McPhate, J.B., Nixon, D., Draper, N., Halcrow, W., Nightingale, J., 2018. Time-of-Flight neutron imaging on IMAT@ISIS: a new user facility for materials science. J. Imaging 4, 47.
Li, W., Zhang, S.Y., Kabra, S., Tremsin, A., Abbey, B., Kirkwood, H., Terret, D., Ndoye, S., McDevitt, E., 2014. Characterisation of residual stress due to fillet rolling on bolts made of a nickel base superalloy. Adv. Mater. Res. 996, 670–675.
Llopart, X., Campbell, M., Dinapoli, R., San Segundo, D., Pernigotti, E., 2002. Medipix2: a 64-k pixel readout chip with 55- m square elements working in single photon counting mode. IEEE Trans. Nucl. Sci. 49, 2279–2283.
Llopart, X., Ballabriga, R., Campbell, M., Tlustos, L., Wong, W., 2007. Timepix, a 65k programmable pixel readout chip for arrival time, energy and/or photon counting measurements. Nucl. Instrum. Methods Phys. Res. 581, 485–494.
Llopart, X., Alozy, J., Ballabriga, R., Campbell, M., Egidos, N., Fernandez, J.M., Heijne, E., Kremastiotis, I., Santin, E., Tlustos, L., Sriskaran, V., Poikela, T., 2019. Study of low power front-ends for hybrid pixel detectors with sub-ns time tagging. J. Inst. Met. 14, C01024.
Long, J., Furch, F., Durá, J., Tremsin, A., Vallerga, J., Schulz, C., Rouzée, A., Vrakking, M., 2017. Ion-ion coincidence imaging at high event rate using an in-vacuum pixel detector. J. Chem. Phys. 147, 013919.
Makowska, M., Strobl, M., Lauridsen, E.M., Frandsen, H.L., Tremsin, A.S., Kardjilov, N., Manke, I., Kelleher, J.F., Theil Kuhn, L., 2015. Effect of stress on NiO reduction in solid oxide fuel cells – a new application of energy-resolved neutron imaging. J. Appl. Crystallogr. 48, 401–408.
Makowska, M.G., Strobl, M., Luridsen, E.M., Kabra, S., Kockelmann, W., Tremsin, A., Frandsen, H.L., Kuhn, L.T., 2016. In-situ time-of-flight neutron imaging of NiO-YSZ reduction under influence of stress. J. Appl. Crystallogr. 49, 1674–1681.
X. Michalet , R. A. Colyer, G. Scalia, A. Ingargiola, R. Lin, J. E. Millaud, S. Weiss, O. H. W. Siegmund, A. S. Tremsin, J. V. Vallerga, A. Cheng, M. Levi, D. Aharoni, K. Arisaka, F. Villa, F. Guerrieri, F. Panzeri, I. Rech, A. Gulinatti, F. Zappa, M. Ghioni, S. Cova, "Development of new photon-counting detectors for single-molecule fluorescence microscopy ", Philos. Trans. R. Soc. Biol. Sci. 368, Issue: 1611, Special Issue: SI, Article Number: 20120035 (2013) DOI: 10.1098/rstb.2012.0035.
Nelson, R.O., Vogel, S.C., Hunter, J., Losko, A.S., Tremsin, A.S., Espy, M., Gautier, C., Williamson, T., Schroeder, K., McClellan, K.J., Nelson, A.T., White, J., Vo, L., Mosby, S., Borges, N.P., Sevanto, Sanna, Madden, A., Winch, N., Mayo, D., Cutler, T., Schirato, R., Alicia, Ramos, K., Montgomery, D., 2018. "Neutron Imaging at LANSCE – from cold to ultrafast". J. Imaging 4, 45.
Nomerotski, A., Chakaberia, I., Fisher-Levine, M., Janoska, Z., Takacsa, P., Tsang, T., 2017. Characterization of TimepixCam, a fast imager for the time-stamping of optical photons. J. Inst. Met. 12, C01017.
Ooi, M., Teshigawara, M., Kai, T., Hadara, M., Maekawa, F., Futakawa, M., Hashimoto, E., Segawa, M., Kureta, M., Tremsin, A., Kamiyama, T., Kiyanagi, Y., 2013. Resonance neutron imaging of the Au-In-Cd alloy at JSNS. Physics Procedia 43, 337–342.
Parker, J.D., Hattori, K., Fujioka, H., Harada, M., Iwaki, S., Kabuki, S., Kishimoto, Y., Kubo, H., Kurosawa, S., Miuchi, K., Nagae, T., 2013. Neutron imaging detector based on the mPIC micro-pixel chamber. Nucl. Instrum. Methods Phys. Res. 697, 23–31.
Perelli Cippo, E., Borella, A., Gorini, G., Kockelmann, W., Moxon, M., Postma, H., Rhodes, N.J., Schillebeeckx, P., Schoonenveld, E.M., Tardocchi, M., Dusz, K., Hajnal, Z., Biro, K., Porcinai, S., Andreanii, C., Festai, G., 2011. Imaging of cultural heritage objects using neutron resonances. J. Anal. At. Spectrom. 26, 992–999.
Poikela, T., Plosila, J., Westerlund, T., Campbell, M., De Gaspari, M., Llopart, X., Gromov, V., Kluit, R., van Beuzekom, M., Zappon, F., Zivkovic, V., Brezina, C., Desch, K., Fu, Y., Kruth, A., 2014. Timepix3: a 65K channel hybrid pixel readout chip with simultaneous ToA/ToT and sparse readout. J. Inst. Met. 9, C05013.
Ramadhan, R.S., Syed, A.K., Tremsin, A.S., Kockelmann, W., Chen, B., Parfitt, D., Fitzpatrick, M.E., 2018. Mapping residual strain induced by cold working and by laser shock peening using neutron transmission spectroscopy. Mater. Des. 143, 56–64.
Sales, M., Strobl, M., Shinohara, T., Tremsin, A., Theil Kuhn, L., Lionheart, W.R.B., Desai, N.M., Bjorholm Dahl, A., Schmidt, S., 2018. Three dimensional polarimetric neutron tomography of magnetic fields. Sci. Rep. 8, 2214.
Santisteban, J.R., Vicente-Alvarez, M.A., Vizcaino, P., Banchik, A.D., Vogel, S.C., Tremsin, A.S., Vallerga, J.V., McPhate, J.B., Lehmann, E., Kockelmann, W., 2012. "Crystallographic texture contrast in neutron radiography of zirconium based components". J. Nucl. Mater. 425, 218–227.
Santodonato, L., Bilheux, H., Bailey, B., Bilheux, J., Nguyen, P., Tremsin, A., Selby, D., Walker, L., 2015. The CG-1D neutron imaging beamline at the Oak Ridge national laboratory high flux isotope reactor. Physics Procedia 69, 104–108.
Sato, H., Sato, T., Shiota, Y., Kamiyama, T., Tremsin, A.S., Ohnuma, M., Kiyanagi, Y., 2015. Relation between vickers hardness and bragg-edge broadening in quenched steel rods observed by pulsed neutron transmission imaging. Mater. Trans. 56, 1147–1152.
Schillebeeckx, P., Borella, A., Emiliani, F., Gorini, G., Kockelmann, W., Kopecky, S., Lampoudis, C., Moxon, M., Perelli Cippo, E., Postma, H., Rhodes, N.J., Schooneveld, E.M., Van Bevereng, C., 2012. Neutron resonance spectroscopy for the characterization of materials and objects. J. Instrum. 7, C03009.
Siegmund, O.H.W., Lampton, M., Bixler, J., Bowyer, S., Malina, R.F., 1986. Operational characteristics of wedge and strip image readout systems. IEEE Trans. Nucl. Sci. 33, 723–727.
Siegmund, O.H.W., Jelinsky, P., Jelinsky, S., Stock, J., Hull, J., Doliber, D., Zaninovich, J., Tremsin, A., Kromer, K., 1999. High-resolution cross delay line detectors for the GALEX mission. Proc. SPIE 3765, 429–440.
Siegmund, O.H.W., Tremsin, A.S., Vallerga, J.V., Abiad, R., Hull, J., 2003. High resolution cross strip anodes for photon counting detectors. Nucl. Instrum. Methods Phys. Res. 504, 177–181.
Siegmund, O.H.W., Vallerga, J.V., McPhate, J., Tremsin, A.S., 2004. Next generation microchannel plate detector technologies for UV Astronomy. Proc. SPIE 5488, 789–800.
Siegmund, O.H.W., McPhate, J.B., Vallerga, J.V., Tremsin, A.S., Frisch, H.E., Elam, J.W., Mane, A.U., Wagner, R.G., 2014. Large area event counting detectors with high spatial and temporal resolution. J. Inst. Met. 9, C04002.
Song, G., Lin, J.Y.Y., Bilheux, J.C., Xie, Q., Santodonato, L.J., Molaison, J.J., Skorpenske, H.D., Dos Santos, A.F.M., Tulk, C.A., An, K., Stoica, A.D., Kirka, M.M., Dehoff, R.R., Tremsin, A., Bunn, J., Sochalski-Kolbus, L.M., Bilheux, H.Z., 2017. Characterization of crystallographic structures using bragg-edge neutron imaging at the spallation neutron source. Journal of Imaging 3, 65.
Strobl, M., Woracek, R., Kardjilov, N., Hilger, A., Wimpory, R., Tremsin, A., Wilpert, T., Schulz, C., Manke, I., Penumadu, D., 2012. Time-of-flight neutron imaging for spatially resolved strain investigations based on Bragg edge transmission at a reactor source". Nucl. Instrum. Methods A 680, 27–34.
Sun, T., Tremsin, A.S., Roy, M.J., Hofmann, M., Prangnell, P.B., Withers, P.J., 2018. Investigation of residual stress distribution and texture evolution in AA7050 stationary shoulder friction stir welded joints. Mater. Sci. Eng. A 712, 531–538.
Tremsin, A.S., Lebedev, G.V., Siegmund, O.H.W., Vallerga, J.V., Hull, J.S., McPhate, J.B., Jozwiak, C., Chen, Y., Guo, J.H., Shen, Z.X., Hussain, Z., 2007. High spatial and temporal resolution photon/electron counting detector for synchrotron radiation research. Nucl. Instrum. Methods A 580, 853–857.
Tremsin, A.S., McPhate, J.B., Kockelmann, W.A., Vallerga, J.V., Siegmund, O.H.W., Feller, W.B., 2009. Energy-resolving neutron transmission radiography at the ISIS pulsed spallation source with a high-resolution neutron counting detector. IEEE Trans. Nucl. Sci. 56 N5, 2931–2937.
Tremsin, A.S., McPhate, J.B., Vallerga, J.V., Siegmund, O.H.W., Feller, W.B., Lehmann, E., February . Improved efficiency of high resolution thermal and cold neutron imaging. In: Vienna Conference on Instrumentation 2010. University of Technology, Vienna, Austria, pp. 415–418. Nucl. Instr. Meth. A 628 (2011).
Tremsin, A.S., Mühlbauer, M.J., Schillinger, B., McPhate, J.B., Vallerga, J.V., Siegmund, O.H.W., Feller, W.B., 2010b. High resolution stroboscopic neutron radiography at the FRM-II ANTARES facility. IEEE Trans. Nucl. Sci. 57, 2955–2962.
Tremsin, A.S., McPhate, J.B., Vallerga, J.V., Siegmund, O.H.W., Feller, W.B., Bilheux, H. Z., Molaison, J.J., Tulk, C.A., Crow, L., Cooper, R.G., Penumadu, D., 2010c. Transmission Bragg edge spectroscopy measurements at ORNL spallation neutron source". J. Phys. Conf. Ser. 251, 012069.
Tremsin, A.S., McPhate, J.B., Vallerga, J.V., Siegmund, O.H.W., Feller, W.B., Lehmann, E., Dawson, M., 2011a. High resolution neutron micro-tomography with noiseless neutron counting detector. Nucl. Instrum. Methods A 652, 400–403.
Tremsin, A.S., McPhate, J.B., Kockelmann, W., Steuwer, A., Vallerga, J.V., Siegmund, O. H.W., Feller, W.B., 2011b. High resolution neutron counting sensors in strain mapping through a transmission Bragg edge diffraction. IEEE Sens. J. 11, 3433–3436.
Tremsin, A.S., McPhate, J.B., Kockelmann, W., Vallerga, J.V., Siegmund, O.H.W., Feller, W.B., 2011c. High resolution Bragg edge transmission spectroscopy at pulsed neutron sources: proof of principle experiments with neutron counting MCP detector. Nucl. Instrum. Methods A 633, S235–S238.
Tremsin, A.S., McPhate, J.B., Vallerga, J.V., Siegmund, O.H.W., Feller, W.B., Lehmann, E., Kaestner, A., Boillat, P., Panzner, T., Filges, U., 2012a. Neutron radiography with sub-15 μm resolution through event centroiding. Nucl. Instrum. Methods A 688, 32–40.

Tremsin, A.S., McPhate, J.B., Steuwer, A., Kockelmann, W., M Paradowska, A., Kelleher, J.F., Vallerga, J.V., Siegmund, O.H.W., Feller, W.B., 2012b. High-resolution strain mapping through time-of-flight neutron transmission diffraction with a microchannel plate neutron counting detector", Strain. Int. J. Exp.Mech. 48, 296–305.

Tremsin, A.S., McPhate, J.B., Vallerga, J.V., Siegmund, O.H.W., Kockelmann, W., Schooneveld, E.M., Rhodes, N.J., Feller, W.B., 2012c. High resolution neutron resonance absorption imaging at a pulsed neutron beamline. IEEE Trans. Nucl. Sci. 59, 3272–3277.

Tremsin, A.S., Vogel, S.C., Losko, A.S., Olinger, C.T., Kockelmann, W., 2019. Non-destructive Studies of Iron and Stony Meteorite Materials by Energy Resolved Neutron Imaging. IEEE Nucl. Sci. Symposium, Manchester, October.

Tremsin, A.S., Vogel, S.C., Mocko, M., Bourke, M.A.M., Yuan, V., Nelson, R.O., Brown, D. W., Feller, W.B., 2013a. Energy resolved neutron radiography at LANSCE pulsed neutron facility. Neutron News 24 (Issue 4), 28–32.

Tremsin, A.S., Vallerga, J.V., McPhate, J.B., Siegmund, O.H.W., Raffanti, R., 2013b. High resolution photon counting with MCP-timepix quad parallel readout operating at > 1KHz frame rates. IEEE Trans. Nucl. Sci. 60, 578–585.

Tremsin, A.S., Vogel, S.C., Mocko, M., Bourke, M.A.M., Yuan, V., Nelson, R.O., Brown, D. W., Feller, W.B., 2013c. Non-destructive studies of fuel rodlets by neutron resonance absorption radiography and thermal neutron radiography. J. Nucl. Mater. 440, 633–646.

Tremsin, A.S., McPhate, J.B., Vallerga, J.V., Siegmund, O.H.W., Feller, W.B., Kockelmann, W., Paradowska, A., Zhang, S.Y., Kelleher, J., Steuwer, A., Santisteban, J., 2014a. High-resolution strain mapping through time-of-flight neutron transmission diffraction. Mater. Sci. Forum 772, 9–13.

Tremsin, A.S., Shinohara, T., Kai, T., Ooi, M., Kamiyama, T., Kiyanagi, Y., Shiota, Y., McPhate, J.B., Vallerga, J.V., Siegmund, O.H.W., Feller, W.B., 2014b. Neutron resonance transmission spectroscopy with high spatial and energy resolution at J-PARC pulsed neutron source. Nucl. Instrum. Methods A 746, 47–58.

Tremsin, A.S., Vallerga, J.V., McPhate, J.B., Siegmund, O.H.W., 2015a. Optimization of high count rate event counting detector with Microchannel Plates and quad Timepix readout. Nucl. Instrum. Methods A 787, 20–25.

Tremsin, A.S., Morgano, M., Panzner, T., Lehmann, E., Filgers, U., Vallerga, J.V., McPhate, J.B., Siegmund, O.H.W., Feller, B., 2015b. High resolution neutron imaging capabilities with MCP/Timepix detector at BOA beamline at PSI". Nucl. Instrum. Methods A 784, 486–493.

Tremsin, A.S., Lehmann, E.H., McPhate, J.B., Vallerga, J.V., Siegmund, O.H.W., White, B., White, P., Feller, W.B., de Beer, F.C., Kockelmann, W., 2015c. Quantification of cement hydration through neutron radiography with scatter rejection. IEEE Trans. Nucl. Sci. 62, 1288–1294.

Tremsin, A.S., Dangendorf, V., Tittelmeier, K., Schillinger, B., Schulz, M., Lerche, M., Feller, W.B., 2015d. Time-resolved neutron imaging at ANTARES cold neutron beamline. J. Instrum.JINST 10, P07008.

Tremsin, A.S., Kardjilov, N., Strobl, M., Manke, I., Dawson, M., McPhate, J.B., Vallerga, J.V., Siegmund, O.H.W., Feller, W.B., 2015e. Imaging of dynamic magnetic fields with spin-polarized neutron beams. New J. Phys. 17, 043047 https://doi.org/10.1088/1367-2630/17/4/043047.

Tremsin, A.S., Kockelmann, W., Pooley, D.E., Feller, W.B., 2015f. Spatially resolved remote measurement of temperature by neutron resonance absorption. Nucl. Instrum. Methods A 803, 15–23.

Tremsin, A.S., Makowska, M.G., Perrodin, D., Shalapska, T., Khodyuk, I.V., Trtik, P., Boillat, P., Vogel, S.C., Losko, A.S., Strobl, M., Theil Kuhn, L., Bizarri, G.A., Bourret-Courchesne, E.D., 2016a. In-situ diagnostics of crystal growth process through neutron imaging: application to scintillators. J. Appl. Crystallogr. 49, 743–755.

Tremsin, A.S., Yau, T.Y., Kockelmann, W., 2016b. Non-destructive examination of loads in regular and self-locking Spiralock® threads through energy-resolved neutron imaging. Strain 52, 548–558.

Tremsin, A.S., Ganguly, S., Meco, S., Pardal, G.R., Shinohara, T., Feller, W.B., 2016c. Non-destructive studies of dissimilar metal welds by energy resolved neutron imaging. J. Appl. Crystallogr. 49, 1130–1140.

Tremsin, A.S., Kockelmann, W., Zhang, Shu-Yan, Korsunsky, A.M., Shinohara, T., Lehmann, E.H., 2016d. Investigation of microstructure within metal welds by energy resolved neutron imaging. J. Phys. Conf. Ser. 746, 012040.

Tremsin, A.S., Gao, Y., Dial, L.C., Grazzi, F., Shinohara, T., 2016e. Investigation of microstructure in additive manufactured Inconel 625 by spatially-resolved neutron transmission spectroscopy. Sci. Technol. Adv. Mater. 17, 324–336.

Tremsin, A.S., Perrodin, D., Losko, A.S., Vogel, S.C., Bourke, M.A.M., Bizarri, G.A., Bourret, E.D., 2017a. Real-time crystal growth visualization and quantification by energy-resolved neutron imaging. Sci. Rep. 7, 46275.

Tremsin, A.S., Perrodin, D., Losko, A.S., Vogel, S.C., Shinohara, T., Oikawa, K., Peterson, J.H., Zhang, C., Derby, J.J., Zlokapa, A.M., Bizarri, G.A., Bourret, E.D., 2017b. In-situ observation of phase separation during growth of Cs2LiLaBr6:Ce crystals using energy-resolved neutron imaging. Cryst. Growth Des. 17, 6372–6381.

Tremsin, A.S., Losko, A.S., Vogel, S.C., Byler, D.D., McClellan, K.J., Bourke, M.A.M., Vallerga, J.V., 2017c. Non-contact measurement of partial gas pressure and distribution of elemental composition using energy-resolved neutron imaging. AIP Adv. 7, 015315.

Tremsin, A.S., Rakovan, J., Shinohara, T., Kockelmann, W., Losko, A.S., Vogel, S.C., 2017d. Non-destructive study of bulk crystallinity and elemental composition of natural gold single crystal samples by energy-resolved neutron imaging. Sci. Rep. 7, 40759.

Tremsin, A.S., Vallerga, J.V., R Raffanti, R., 2018a. Optimization of spatial resolution and detection efficiency for photon/electron/neutron/ion counting detectors with Microchannel Plates and Quad Timepix readout. J. Instrum.JINST 13, C11005.

Tremsin, A.S., Kockelmann, W., Kelleher, J.F., Paradowska, A.M., Ramadhan, R.S., Fitzpatrick, M.E., 2018b. Energy-resolved neutron imaging for reconstruction of strain introduced by cold working. J. Imaging 4, 48.

Tremsin, A.S., Craft, A.E., Bourke, M.A.M., Smolinski, A.T., Papaioannou, G.C., Ruddell, M.A., Littell, J., Tedesco, J., 2018c. Digital neutron and gamma-ray radiography in high radiation environments with an MCP/Timepix detector. Nucl. Instrum. Methods Phys. Res. 902, 110–116.

Tremsin, A.S., Shinohara, T., Oikawa, K., Li, Jiaqi, Monteiro, P.J.M., 2019a. Non-destructive mapping of water distribution through white-beam and energy-resolved neutron imaging. Nucl. Instrum. Methods Phys. Res. 927, 174–183.

Tremsin, A.S., Craft, A.E., Papaioannou, G.C., Smolinski, A.T., Boulton, N.M., Ruddell, M. A., Littell, B.J., Riley, K.D., 2019b. On the possibility to investigate irradiated fuel pins non-destructively by digital neutron radiography with a neutron-sensitive microchannel plate detector with Timepix readout. Nucl. Instrum. Methods Phys. Res. 927, 109–118.

Turecek, D., Holy, T., Jakubek, J., Pospisil, S., Vykydal, Z., 2011. Pixelman: a multi-platform data acquisition and processing software package for Medipix2, Timepix and Medipix3 detectors. J. Instrum. 6, 1–6.

Vallerga, J.V., McPhate, J., Mikulec, B., Tremsin, A., Clark, A., Siegmund, O., 2004. Noiseless imaging detector for adaptive optics with kHz frame rates. In: Proc. SPIE Vol. 5490 "Advancements in Adaptive Optics", Glasgow, pp. 1256–1267.

Vallerga, J.V., McPhate, J.B., Tremsin, A.S., Siegmund, O.H.W., Mikulec, B., Clark, A.G., 2005a. Optically sensitive Medipix2 detector for adaptive optics wavefront sensing. Nucl. Instrum. Methods A 546/1–2, 263–269.

Vallerga, J.V., Tremsin, A.S., McPhate, J.B., Mikulec, B., Clark, A.G., Siegmund, O.H., 2005b. In: Tyson, Robert K., Lloyd-Hart, Michael (Eds.), "Photon-counting Arrays for AO Wavefront Sensor Detectors", Proc. SPIE Vol. 5903, "Astronomical Adaptive Optics Systems and Applications II". San Diego August, pp. 160–170, 2005.

Vallerga, J., Tremsin, A., DeFazio, J., Alozy, J., Tick, T., 2014. Optical MCP image tube with a quad Timepix readout: initial performance characterization. J. Instrum.JINST 9, C05055.

Vitucci, G., Minniti, T., Di Martino, D., Musa, M., Gori, L., Micieli, D., Kockelmann, W., Watanabe, K., Tremsin, A.S., Gorini, G., 2018. Energy-resolved (4D) neutron tomography of an unconventional bead cultured pearl at a pulsed spallation source using a microchannel plate camera. Microchem. J. 137, 473–479.

Wensrich, C.M., Hendriks, J.N., Gregg, A., Meylan, M.H., Luzin, V., Tremsin, A.S., 2016. Bragg-edge neutron transmission strain tomography for in situ loadings. Nucl. Instrum. Methods Phys. Res. B 383, 52–58.

Wiza, J.L., 1979. Microchannel plate detectors. Nucl. Instrum. Methods 162, 587–601.

Woracek, R., Bunn, J., Penumadu, D., Tremsin, A., Kardjilov, N., Manke, I., Hubbard, C., Cady, B., Claussen, B., Sisneros, T., 2013. Measurement of hkl strains under complex loading paths and methodology for combined neutron diffraction and imaging. Mater. Res. Soc. Symp. Proc. 1528 https://doi.org/10.1557/opl.2013.571. Materials Research Society.

Yuan, V.W., Bowman, J.D., Funk, D.J., Morgan, G.L., et al., 2005. Shock temperature measurement using neutron resonance spectroscopy. Phys. Rev. Lett. 94, 125504.

Zhao, A., van Beuzekom, M., Bouwens, B., Byelov, D., Chakaberia, I., Cheng, C., Maddox, E., Nomerotski, A., Svihra, P., Visser, J., Vrba, V., Weinacht, T., 2017. Coincidence velocity map imaging using Tpx3Cam, a time stamping optical camera with 1.5 ns timing resolution. Rev. Sci. Intr. 88, 113104.